Renal clearable catalytic gold nanoclusters for *in vivo* disease monitoring

Colleen N. Loynachan[†1], Ava P. Soleimany[†2,3], Jaideep S. Dudani[2,4], Yiyang Lin[1], Adrian Najer[1], Ahmet Bekdemir[2], Qu Chen[1], Sangeeta N. Bhatia[*2,5-9], Molly M. Stevens[*1]

†***Contributed equally*, **co-corresponding authors***

1. Department of Materials, Department of Bioengineering, and Institute of Biomedical Engineering, Imperial College London, London SW7 2AZ, London, U.K.
2. Koch Institute for Integrative Cancer Research, Massachusetts Institute of Technology, Cambridge, MA 02139
3. Harvard Graduate Program in Biophysics, Harvard University, Boston, MA 02115
4. Department of Biological Engineering, Massachusetts Institute of Technology, Cambridge, MA 02139
5. Harvard-MIT Division of Health Sciences and Technology, Institute for Medical Engineering and Science, Massachusetts Institute of Technology, Cambridge, MA 02139
6. Department of Electrical Engineering and Computer Science, Massachusetts Institute of Technology, Cambridge, MA 02139
7. Department of Medicine, Brigham and Women's Hospital and Harvard Medical School, Boston, MA 02115
8. Broad Institute of Massachusetts Institute of Technology and Harvard, Cambridge, MA 02139
9. Howard Hughes Medical Institute, Cambridge, MA 02139

Email: sbhatia@mit.edu and m.stevens@imperial.ac.uk

ABSTRACT

Ultra-small gold nanoclusters (AuNCs) have emerged as agile probes for *in vivo* imaging, as they exhibit exceptional tumour accumulation and efficient renal clearance properties. However, their intrinsic catalytic activity, which can enable increased detection sensitivity, has yet to be explored for *in vivo* sensing. By exploiting the peroxidase-mimicking activity of AuNCs and the precise nanometer size filtration of the kidney, we designed multifunctional protease nanosensors that respond to disease microenvironments to produce a direct colorimetric urinary readout of disease state in less than 1 h. We monitored the catalytic activity of AuNCs in collected urine of a mouse model of colorectal cancer where tumour-bearing mice showed a 13-fold increase in colorimetric signal compared to healthy mice. Nanosensors were eliminated completely through hepatic and renal excretion within 4 weeks after injection with no evidence of toxicity. We envision that this modular approach will enable rapid detection of a diverse range of diseases by exploiting their specific enzymatic signatures.

KEYWORDS

catalytic nanoparticles, nanoclusters, biosensing, enzyme-mimic, biorthogonal chemistry, renal clearance, activity-based biomarkers, proteases, nanosensors, urinary diagnostic

MAIN

Democratization of diagnostic tools to enable simple, sensitive, and early detection of disease is essential, particularly in low- and middle-income countries, which bear a significant burden of both infectious and noncommunicable diseases.[1] While worldwide mortality rates due to infectious diseases have substantially decreased, the ever increasing ageing population means cancer has become a primary cause of morbidity and mortality.[2] New globally accessible diagnostic tools will be key in addressing unmet challenges in global oncology. Advances in nanotechnology offer unprecedented solutions in the form of responsive detection tools that, when applied globally, can enable earlier diagnosis and better treatment irrespective of the local resources available.[3]

Early diagnosis of cancer enables effective treatment of primary tumours via local therapeutic interventions such as surgery and radiotherapy.[4] Early detection has largely relied on blood biomarkers. However, the prohibitively low rates that most biomarkers are shed from tumours, the tremendous dilution into circulation, and the lack of specificity of secreted biomarkers impede early detection.[5,6] Protease activities are implicated in a wide range of noncommunicable human diseases including cancer, inflammation, and thrombosis. Monitoring protease activity as a biomarker of disease may be leveraged to overcome the lack of sensitivity and specificity of abundance-based blood biomarkers.[7] Common tools to measure protease activity often rely on cumbersome and infrastructure heavy analyses, such as fluorescence,[8–10] mass spectrometry,[11] or MRI.[12] Previously, we developed exogenously administered multiplexed protease-responsive nanoparticles that release small reporter probes into the urine in response to proteolytic cleavage in disease environments.[3,13–15] These protease nanosensors offer sensitivity advantages for *in vivo* protease monitoring due to enzymatic amplification and renal concentration of reporter probes from blood to urine, allowing for direct measurement of reporters by mass spectrometry[16] or immunoassays.[13,17] In practice, however, these techniques require analysis and expensive analytical reagents not typically available in resource-limited settings. For precision medicine to become globally accessible, diagnostic tools that can probe protease activity with a simple and sensitive readout are required.

Ultra-small gold nanoclusters (AuNCs, < 2 nm) offer an elegant solution to the need for simple and sensitive diagnostic readouts due to their discrete electronic and molecular-like properties.[18,19] Particularly, noble metal nanoclusters and nanoparticles can function as catalysts to disproportionate or decompose H_2O_2, which in turn can oxidise a chromogenic substrate, providing a colorimetric measure of catalytic activity, similar to the enzyme

horseradish peroxidase (HRP).[20–22] Despite this potential to provide a high sensitivity and simple readout for early disease detection, to date AuNCs have been used *in vivo* solely for fluorescence and X-ray contrast bioimaging applications.[23–25] We therefore sought to leverage the catalytic activity of AuNCs to develop a nanosensor platform that produces a direct colorimetric readout of disease state.

Here, we present the design of a versatile and modular nanosensor, comprised of renal clearable catalytic AuNCs tethered via peptide linkages to a larger protein carrier, that is disassembled in response to dysregulated protease activity at the site of disease. To demonstrate the modularity of the system in responding to different families of proteases, we synthesized functionalised peptide substrates shown to be specifically cleaved by either the serine protease thrombin[26,27] or the zinc-dependent matrix metalloproteinase 9 (MMP9), which play a critical role in cardiovascular disease or cancer, respectively.[28,29] We demonstrated the response of our protease nanosensors both *in vitro* and *in vivo*, achieving sensitive disease detection with a rapid, colorimetric urinary readout in a mouse model of colorectal cancer using our MMP-responsive nanosensors. Our system exhibited a dual amplification platform: leveraging both *in vivo* protease activity and inorganic catalytic activity of AuNCs to provide a visual readout of disease state directly in urine. With this method, we demonstrate that these AuNCs are small enough to be filtered efficiently through the kidneys and retain catalytic activity in cleared urine, thus providing a versatile disease detection platform that is compatible for deployment at the point-of-care (PoC).

Peptide-templated catalytic AuNCs with high serum stability

Protease responsive nanosensors were synthesized using biotinylated protease-cleavable peptides to template and stabilize the growth of catalytic AuNCs, which were further coupled to neutravidin (NAv). Neutravidin was selected as a biocompatible carrier for protease-responsive AuNC reporter probes due to its high affinity for biotin and low nonspecific binding properties (Fig. 1).[30] The AuNC-neutravidin (AuNC-NAv) complex was then intravenously administered and specifically disassembled by proteases at the site of disease. Our system takes advantage of a biological pharmacokinetic switch, where the size of the particle largely drives biodistribution.[31,32] Once proteolytically liberated from the neutravidin complex, AuNCs circulated via the bloodstream and were efficiently filtered into the urine through the kidneys due to their small size (< 5 nm). A simple colorimetric assay was performed on the urine to assess the presence of AuNCs as an indicator of disease state (Fig. 1).

We used a co-templated approach to synthesize noble metal nanoclusters, incorporating both the tripeptide glutathione (GSH, γ-Glu–Cys–Gly), a common capping ligand in nanocluster synthesis,[23,33] and a thiol-terminated functional protease-cleavable peptide (Table 1) that act as both stabilizing capping ligands and reducing agents for nanoparticle formation (Fig. 2a). Gold was selected as the core metal, as it exhibited the highest catalytic activity compared to platinum and gold-platinum bimetallic hybrid nanoclusters and could be produced with a low coefficient of variation (CoV = 8.5%), an important consideration in designing a scalable diagnostic platform (Supplementary Fig. 1).

The peptide substrates used as templates for AuNC synthesis were composed of three functional domains: an enzyme recognition motif, a C-terminal cysteine residue to provide a thiol group for sequestering Au ions, and an N-terminal biotin ligand for efficient conjugation to a neutravidin carrier protein. The advantage of this synthesis route to produce catalytic noble metal nanoclusters is the ability to incorporate responsive and functional ligands onto the surface through simple gold-thiol interactions in a one-pot synthesis. Additionally, we have previously investigated carrier and linker-specific effects on cleavage rates,[14] and hypothesized that the target protease may be sterically hindered from accessing the scissile bond when the peptide sequence is presented on the AuNC and simultaneously linked to the neutravidin core. To explore this hypothesis, we also synthesized longer peptides ($P1_{20}$, $P2_{20}$) by incorporating glycine spacers between the N-terminus and protease recognition motif (Table 1). We assessed the ability of the relevant protease to cleave the peptide substrate by verifying the mass of fragments after *in vitro* protease degradation (Supplementary Fig. 2).

The AuNCs did not exhibit surface plasmon resonance, a characteristic of large gold nanoparticles, but rather exhibited molecular-like absorption and corresponding fluorescence properties, attributed to the discrete electronic state arising from their size (Supplementary Fig. 3). Transmission electron microscope (TEM) images and size analysis of the peptide-templated AuNCs (Fig. 2b, Supplementary Figs. 4 and 5) showed that the average size (1.5 ± 0.4 nm, Fig 2c) was below the glomerular filtration cut-off (*ca*. 5.5 nm), making them ideally suited for kidney clearance.[31,32,34–36]

The peroxidase-like catalytic activity of the resulting AuNCs was measured using the oxidation of the peroxidase substrate 3,3′,5,5′-Tetramethylbenzidine (TMB) by H_2O_2 as a model catalytic reaction, and absorbance at 652 nm provided a colorimetric readout of AuNC activity (Fig. 2d, Supplementary Fig. 1 and 6, Supplementary Table 2). To assess the sensitivity of our catalytic reporter probes, we measured the catalytic activity of a dilution series of each AuNC batch in synthetic urine (Fig. 2e) and determined the limit of detection to be *ca*. 2.7 picomoles (25 µL urine, *ca.* 100 nM AuNCs), with a broad linear response and dynamic range spanning over three orders of magnitude of particle concentration.

There are several advantages to using inorganic AuNCs over natural peroxidases. HRP is not feasible to use as a reporter probe in a comparable *in vivo* diagnostic system, as it is not readily cleared through the renal filtration pathway due to its size (*ca*. 4.5 nm) and the tendency for proteins to be reabsorbed by the tubular epithelium.[37] Additionally, HRP would be susceptible to nonspecific degradation by endogenous proteases *in vivo* which would hinder activity of any cleared enzyme.[38] On the other hand, AuNCs showed high stability in physiological environments, maintaining catalytic activity, size, and morphology in the presence of serum, urine, and physiologically relevant glutathione concentrations (Fig. 2f, Supplementary Figs. 7, 8, and 9). A key performance requirement of the AuNCs is that they retain their catalytic activity following exposure to complex environments such as patient serum, which contains *ca*. 7 wt% protein. AuNCs effectively evaded nonspecific protein adsorption, retaining 80 – 90% of catalytic activity after 1 h incubation in fetal bovine serum (undiluted FBS) or synthetic urine compared to PBS controls (Fig. 2f). In deciding which particle platform to take forward *in vivo*, we selected a system that balanced appropriate protease substrate loading with retention of activity (Supplementary Fig. 10).

Renal clearance of AuNCs and activity retention in urine

The high physiological stability and retention of AuNC catalytic activity after exposure to serum and urine offered a unique opportunity to non-invasively measure AuNC clearance in urine

using both intrinsic catalytic activity and gold content with inductively coupled mass spectrometry (ICP-MS) (Fig. 3a). To determine renal clearance efficiency, urine from mice injected with AuNCs was measured against a calibration curve for both catalytic activity and gold content. This showed that up to 73 ± 7% of the injected dose of functionalised AuNCs left the body via this route at 1 h post injection (p.i.) and retained catalytic activity in urine (Fig. 3b). Encouragingly, the catalytic activity assay and ICP-MS results appeared to correlate (Fig. 3c, Pearson's r = 0.492, $*P$ = 0.0383). Thus, the catalytic activity assay can provide a simple and sensitive assessment of AuNC presence in urine without the need for ICP-MS. Analysis of urine from mice injected with PBS revealed that no endogenous peroxidase activity was detectable in collected urine (Supplementary Fig. 11). Using TEM image analysis, we confirmed that the size and morphology of AuNCs cleared by the kidneys and excreted into the urine was comparable to as-synthesized AuNCs (Supplementary Fig. 8). This indicates that the particle stability was unperturbed *in vivo*, which is consistent with the retention of the functional properties of the nanoclusters after *in vivo* interrogation.

AuNC nanosensors respond to protease activity *in vitro*

The biotin functional handles on the protease substrate-modified AuNCs were used to tether them to a neutravidin carrier protein to assemble an AuNC-NAv complex. Dynamic light scattering (DLS) was used to monitor the size of the free AuNCs, neutravidin carrier, and assembled AuNC-NAv complex (Supplementary Figs. 12 and 13), with representative hydrodynamic diameters of 2.5 ± 0.6 nm (GSH-AuNC), 3.3 ± 0.7 nm (AuNC-$P1_{20}$), 7.9 ± 1.5 nm (NAv), and 11.3 ± 2.2 nm (AuNC-$P1_{20}$-NAv).

To explore the kinetics of proteolytic cleavage of AuNC-NAv complexes, we employed fluorescence correlation spectroscopy (FCS) as a single-molecule detection method (Fig. 4a). After enzyme incubation, the diffusivity of the complex shifted over time towards that of the free fluorescently labelled clusters, indicating cleavage had occurred (Fig. 4b). Hydrodynamic size analysis by FCS showed that the MMP-responsive AuNC-$P2_{20}$-NAv complex was completely disassembled within 4.5 h of MMP9 incubation (Fig. 4c). The size of the thrombin-cleavable complex, AuNC-$P1_{20}$-NAv, did not significantly change when incubated with MMP9, and the size of the MMP-responsive AuNC-$P2_{20}$-NAv complex did not fall below the renal filtration limit when incubated with an off-target enzyme, in this case thrombin, for 12 h. Taken together, these results show the specificity of our nanosensors for their target enzymes. To demonstrate the modularity of our system, we used FCS to measure the disassembly kinetics of the thrombin-responsive complex (AuNC-$P1_{20}$-NAv), which was efficiently cleaved by thrombin (Supplementary Fig. 14). Further, MMP9 exhibited a rate of 3% AuNC cleaved per

minute toward the AuNC-$P2_{20}$-NAv complex, while the rate was only 0.08% AuNC cleaved per minute toward the AuNC-$P2_{13}$-NAv complex (Fig. 4d). This *ca*. 40-fold increase in the cleavage rate for the complex formed with the longer linker could be attributed to increased accessibility of the enzyme to the scissile bond. FCS results showed that in the presence of biologically-relevant enzyme concentrations,[39] significant cleavage was observed for AuNC-$P2_{20}$-NAv complexes, where 80% of AuNCs were cleaved within the first hour of incubation with MMP9.

Proteolytic cleavage of AuNC-NAv complexes was further characterized *in vitro* by incubating complexes with recombinant protease, using gel filtration chromatography (GFC) to separate cleavage products by size, and monitoring cleavage with a catalytic activity assay (Supplementary Fig. 13). The extent of cleavage of the AuNC-NAv complex under different conditions was quantified by analysing the area under the curve associated with each cleavage product from the activity assay (Supplementary Table 3). Non-specific cleavage was investigated by incubating AuNC-$P1_{20}$-NAv with MMP9 and AuNC-$P2_{20}$-NAv with thrombin. Low background cleavage by the off-target enzyme was observed (Fig. 4e-f), in agreement with FCS results. Finally, we explored the sensitivity of our nanosensor to MMP9 activity *in vitro* using both FCS and a filtration-based colorimetric catalytic activity assay (Supplementary Fig. 15), where low nanomolar sensitivities were observed, comparable to commercial *in vitro* fluorogenic protease activity assays.

Biodistribution and clearance pathways for nanosensors

We assessed the biocompatibility of AuNC-NAv complexes *in vitro* and found that they were non-toxic to HEK293T cells up to 15 µM (Supplementary Fig. 16). Toxicological responses of our AuNC-NAv complexes (3000 pmol AuNC dose) *in vivo* was investigated by examining pathology of the mice after complex injection. No significant changes in bodyweight over 28 days and no histological evidence of heart, lung, liver, spleen, or kidney toxicity were found at both short (1 h) and longer (24 h and 10 days) time points post injection, suggesting that AuNC-NAv complexes did not induce significant systemic toxicity (Supplementary Fig. 16).

To assess clearance time frames and mechanisms, we explored the organ biodistribution, blood pharmacokinetics, urine composition, and elimination pathways of AuNCs and AuNC-NAv complexes labelled with a photostable near-IR dye. From the organ biodistribution study, free AuNCs accumulated most significantly in the kidneys relative to other organs including the liver at 1 h p.i. and were completely cleared from all major organs within 7 days p.i. To corroborate the biodistribution study, we measured gold signal in the urine by ICP-MS and our catalytic activity assay, where the presence of AuNCs was undetectable after 24 h p.i.

(Supplementary Fig. 17, Supplementary Table 4). Due to their size (*ca*. 11 nm), the intact AuNC-NAv complexes accumulated predominately in reticuloendothelial system (RES) organs.[40] The AuNC-NAv signal in the liver increased up to 24 h p.i., significantly decreased after 1 week, and was completely undetectable in all major organs 4 weeks p.i. (Supplementary Fig. 18). Encouragingly, the biodistribution and histology results suggest that, in healthy animals, intact AuNC-NAv complexes were cleared from the circulation and taken up in RES organs and eliminated completely through hepatic (bile to faeces) and renal (urine) excretion within 4 weeks p.i. with no evidence of systemic or tissue-level toxicity.

AuNC nanosensors enable colorimetric urinary disease detection

After confirming successful cleavage by recombinant proteases *in vitro*, we sought to apply the protease responsive AuNC nanosensor platform to *in vivo* disease detection using the colorimetric urinary readout. We characterized the pharmacokinetics of the neutravidin carrier, AuNC-NAv complex, and free AuNCs in terms of accumulation in organs and tumour xenografts of the human colorectal cancer cell line LS174T, which secretes MMP9[13] (Supplementary Fig. 19). Based on the measured blood half-life of the AuNC-NAv complex and the degree of tumour accumulation within 1 h p.i., we selected 1 h after nanosensor injection as our time point for urine collection.

For *in vivo* tumour detection experiments, tumour-bearing and healthy control mice were intravenously injected with MMP-responsive AuNC-$P2_{20}$-NAv nanosensors (Fig. 5a). Urine was collected from mice 1 h p.i., and the catalytic activity assay was run using 25 µL of urine sample. Comparing signal from healthy and tumour-bearing mice, we observed a blue colour that could be read by eye in urine samples from tumour-bearing mice after the addition of the chromogenic peroxidase substrate, TMB (Fig. 5b). Quantification revealed a mean urinary signal increase of approximately 13-fold in tumour-bearing mice relative to healthy mice, as measured by the direct colorimetric readout and initial rate analysis (A_{652} min^{-1}) of cleared AuNC catalytic activity in collected urine (Fig. 5c). The AuNC catalytic activity measured corresponded to *ca*. 3.2% of the injected dose in urine from tumour-bearing mice compared to 0.2% renal clearance in healthy mice, normalized using urine volumes (Supplementary Fig. 20). We believe our platform might benefit from improved diffusion, transport, tumour accumulation, and clearance properties of peptide-templated gold nanoclusters compared to larger nanomaterials commonly used in delivery applications, where only *ca*. 0.7% of the administered nanoparticle dose was reported to be delivered to the solid tumour.[41–43] Receiver operating characteristic (ROC) analysis revealed that the colorimetric test was highly accurate and discriminated the presence of colorectal cancer xenografts with an area under the curve

(AUC) of 0.91 (Fig. 5d, $P = 0.0002$). Furthermore, the delivery of our nanosensors to malignant tissues can be enhanced by exploiting our one-pot synthesis scheme for the incorporation of active targeting ligands, *e.g.*, the integrin-targeting ligand iRGD,[14] onto the surface of the AuNCs.

Having established that the MMP-responsive AuNC nanosensors could discriminate between tumour-bearing and healthy mice, we sought to assess whether the urinary signal was driven by disease-associated protease activity. There was no significant difference in urine volumes between the groups, and analysis of urine samples from PBS-injected healthy and tumour-bearing mice confirmed that no endogenous peroxidase activity was present in the absence of injected nanosensors (Supplementary Fig. 20). TEM image analysis of urine from tumour-bearing mice confirmed the presence of AuNCs cleared by the kidney, with size and morphology comparable to as-synthesized AuNCs (Supplementary Fig. 8c). To ensure that the AuNC-NAv complex was not disassembling *in vivo* due to poor chemical stability or nonspecific cleavage, we tested a substrate that we did not expect to be specifically cleaved in the tumour model.[17] Thrombin-responsive AuNC-$P1_{20}$-NAv complexes were injected into tumour-bearing and healthy mice and did not result in any significant colorimetric signal in urine from tumour-bearing mice compared to healthy controls (Fig. 5e). This pattern suggested that there is a non-promiscuous release of AuNCs *in vivo* from AuNC-$P2_{20}$-NAv complexes that is amplified in tumour-bearing mice, where elevated MMP levels at the site of disease and in circulation may actively disassemble AuNC-NAv complexes. Taken together, these results demonstrate that the AuNC-NAv nanosensors respond to disease-specific proteolytic activity *in vivo* and enable a direct colorimetric readout of disease state, as evidenced by highly accurate discrimination in a flank tumour model of human colorectal cancer.

CONCLUSIONS

We have developed a modular approach for rapid detection of a disease state based on a simple and sensitive colorimetric urinary assay that requires minimal equipment and can be read by eye in < 1 h. We synthesized *ca*. 2 nm catalytic gold nanocluster probes modified with orthogonal protease substrates, which are responsive to multiple enzymes. We demonstrated that the peptide templated AuNCs can be filtered through the kidneys and excreted into the urine with high efficiency and retain catalytic activity in complex physiological environments. We assembled the AuNC probes into larger complexes, which were disassembled in response to specific proteases. Finally, we deployed MMP-responsive AuNC-NAv complexes *in vivo* in a colorectal cancer mouse model and successfully detected AuNCs in urine from tumour bearing mice with a facile colorimetric readout.

Here, we have shown that through rational surface modification of AuNCs, we can engineer nanosensors that can be deployed *in vivo* and exploit intrinsic catalytic activity of renal clearable noble metal nanoclusters as a disease indicator. We present a versatile toolbox that can be used to probe the complex enzymatic profiles of specific disease microenvironments, the results of which will open new opportunities for developing translatable responsive and catalytic nanomaterial diagnostics for a range of diseases in which enzyme activity can be used as a biomarker. We envision that clinical application of this technology may additionally take advantage of multiplexed protease substrate linkages, such as those responsive to Boolean logic operations,[44,45] which may be able to profile the activities of proteases of diverse classes in order to distinguish between cancer and other pathologies. Our adaptable nanocatalyst amplification platform will be applicable in low-resource settings for rapid detection of a diverse range of disease-associated proteases, including those implicated in infectious diseases, and will democratize access to advanced and sensitive diagnostics.

REFERENCES

1. World Health Organization. *Global action plan for the prevention and control of noncommunicable diseases 2013-2020*. (2013).
2. Selmouni, F. *et al.* Tackling cancer burden in low-income and middle-income countries: Morocco as an exemplar. *Lancet Oncol.* **19**, e93–e101 (2018).
3. Kwon, E. J., Lo, J. H. & Bhatia, S. N. Smart nanosystems: Bio-inspired technologies that interact with the host environment. *Proc. Natl. Acad. Sci.* **112**, 14460–14466 (2015).
4. Etzioni, R. *et al.* The case for early detection. *Nat. Rev. Cancer* **3**, 235 (2003).
5. Hori, S. S. & Gambhir, S. S. Mathematical Model Identifies Blood Biomarker-Based Early Cancer Detection Strategies and Limitations. *Sci. Transl. Med.* **3**, 109ra116 (2011).
6. Henry, N. L. & Hayes, D. F. Cancer biomarkers. *Mol. Oncol.* **6**, 140–146 (2012).
7. Lopez-Otin, C. & Bond, J. S. Proteases: Multifunctional Enzymes in Life and Disease. *J. Biol. Chem.* **283**, 30433–30437 (2008).
8. Hilderbrand, S. A. & Weissleder, R. Near-infrared fluorescence: application to in vivo molecular imaging. *Curr. Opin. Chem. Biol.* **14**, 71–79 (2010).
9. Whitney, M. *et al.* Ratiometric activatable cell-penetrating peptides provide rapid in vivo readout of thrombin activation. *Angew. Chemie - Int. Ed.* **52**, 325–330 (2013).
10. Whitley, M. J. *et al.* A mouse-human phase 1 co-clinical trial of a protease-activated fluorescent probe for imaging cancer. *Sci. Transl. Med.* **8**, (2016).
11. Yepes, D. *et al.* Multiplex profiling of tumor-associated proteolytic activity in serum of colorectal cancer patients. *Proteomics - Clin. Appl.* **8**, 308–316 (2014).
12. Choi, J. S. *et al.* Distance-dependent magnetic resonance tuning as a versatile MRI sensing platform for biological targets. *Nat. Mater.* **16**, 537–542 (2017).
13. Warren, A. D., Kwong, G. A., Wood, D. K., Lin, K. Y. & Bhatia, S. N. Point-of-care diagnostics for noncommunicable diseases using synthetic urinary biomarkers and paper microfluidics. *Proc. Natl. Acad. Sci. U. S. A.* **111**, 3671–6 (2014).
14. Kwon, E. J., Dudani, J. S. & Bhatia, S. N. Ultrasensitive tumour-penetrating nanosensors of protease activity. *Nat. Biomed. Eng.* **1**, 0054 (2017).
15. Schuerle, S., Dudani, J. S., Christiansen, M. G., Anikeeva, P. & Bhatia, S. N. Magnetically Actuated Protease Sensors for in Vivo Tumor Profiling. *Nano Lett.* **16**, 6303–6310 (2016).
16. Kwong, G. A. *et al.* Mass-encoded synthetic biomarkers for multiplexed urinary monitoring of disease. *Nat. Biotechnol.* **31**, 63–70 (2013).
17. Dudani, J. S., Buss, C. G., Akana, R. T. K., Kwong, G. A. & Bhatia, S. N. Sustained-Release Synthetic Biomarkers for Monitoring Thrombosis and Inflammation Using Point-of-Care Compatible Readouts. *Adv. Funct. Mater.* **26**, 2919–2928 (2016).
18. Jin, R. Quantum sized, thiolate-protected gold nanoclusters. *Nanoscale* **2**, 343–362 (2010).
19. Jin, R., Zeng, C., Zhou, M. & Chen, Y. Atomically Precise Colloidal Metal Nanoclusters and Nanoparticles: Fundamentals and Opportunities. *Chem. Rev.* **116**, 10346–10413 (2016).
20. Xia, X. *et al.* Pd-Ir Core-Shell Nanocubes: A Type of Highly Efficient and Versatile Peroxidase Mimic. *ACS Nano* **9**, 9994–10004 (2015).
21. Loynachan, C. N. *et al.* Platinum Nanocatalyst Amplification: Redefining the Gold Standard for Lateral Flow Immunoassays with Ultrabroad Dynamic Range. *ACS Nano* **12**, 279–288 (2018).
22. Tao, Y., Li, M., Ren, J. & Qu, X. Metal nanoclusters: novel probes for diagnostic and therapeutic applications. *Chem. Soc. Rev.* **44**, 8636–8663 (2015).
23. Zhang, X.-D. *et al.* Ultrasmall glutathione-protected gold nanoclusters as next generation radiotherapy sensitizers with high tumor uptake and high renal clearance. *Sci. Rep.* **5**, 8669 (2015).
24. Chen, Y. *et al.* Shortwave Infrared in Vivo Imaging with Gold Nanoclusters. *Nano Lett.*

17, 6330–6334 (2017).
25. Yang, W., Guo, W., Chang, J. & Zhang, B. Protein/peptide-templated biomimetic synthesis of inorganic nanoparticles for biomedical applications. *J. Mater. Chem. B* **5**, 401–417 (2017).
26. Davie, E. W. & Kulman, J. D. An Overview of the Structure and Function of Thrombin. *Semin. Thromb. Hemost.* **32**, 3–15 (2006).
27. ten Cate, H. & Hemker, H. C. Thrombin Generation and Atherothrombosis: What Does the Evidence Indicate? *J. Am. Heart Assoc.* **5**, 1–8 (2016).
28. Roy, R., Yang, J. & Moses, M. A. Matrix metalloproteinases as novel biomarkers and potential therapeutic targets in human cancer. *J. Clin. Oncol.* **27**, 5287–5297 (2009).
29. Dudani, J. S., Warren, A. D. & Bhatia, S. N. Harnessing Protease Activity to Improve Cancer Care. *Annu. Rev. Cancer Biol.* **2**, 53–76 (2018).
30. Jain, A., Barve, A., Zhao, Z., Jin, W. & Cheng, K. Comparison of Avidin, Neutravidin, and Streptavidin as Nanocarriers for Efficient siRNA Delivery. *Mol. Pharm.* **14**, 1517–1527 (2017).
31. Soo Choi, H. *et al.* Renal clearance of quantum dots. *Nat. Biotechnol.* **25**, 1165–1170 (2007).
32. Du, B., Yu, M. & Zheng, J. Transport and interactions of nanoparticles in the kidneys. *Nat. Rev. Mater.* **3**, 358–374 (2018).
33. Luo, Z. *et al.* From aggregation-induced emission of Au(I)-thiolate complexes to ultrabright Au(0)@Au(I)-thiolate core-shell nanoclusters. *J. Am. Chem. Soc.* **134**, 16662–16670 (2012).
34. Yu, M. *et al.* Noninvasive Staging of Kidney Dysfunction Enabled by Renal-Clearable Luminescent Gold Nanoparticles. *Angew. Chemie - Int. Ed.* **55**, 2787–2791 (2016).
35. Ning, X. *et al.* Physiological stability and renal clearance of ultrasmall zwitterionic gold nanoparticles: Ligand length matters. *APL Mater.* **5**, (2017).
36. Liu, J. *et al.* Passive tumor targeting of renal-clearable luminescent gold nanoparticles: Long tumor retention and fast normal tissue clearance. *J. Am. Chem. Soc.* **135**, 4978–4981 (2013).
37. Straus, W. Renal reabsorption and excretion of horseradish peroxidase. *Kidney Int.* **16**, 404–408 (1979).
38. Manning, M. C., Chou, D. K., Murphy, B. M., Payne, R. W. & Katayama, D. S. Stability of protein pharmaceuticals: An update. *Pharm. Res.* **27**, 544–575 (2010).
39. Kwong, G. A. *et al.* Mathematical framework for activity-based cancer biomarkers. *Proc. Natl. Acad. Sci.* **112**, 12627–12632 (2015).
40. Yu, M. & Zheng, J. Clearance Pathways and Tumor Targeting of Imaging Nanoparticles. *ACS Nano* **9**, 6655–6674 (2015).
41. Dai, Q. *et al.* Quantifying the Ligand-Coated Nanoparticle Delivery to Cancer Cells in Solid Tumors. *ACS Nano* **12**, 8423–8435 (2018).
42. Tang, S. *et al.* Tailoring Renal Clearance and Tumor Targeting of Ultrasmall Metal Nanoparticles with Particle Density. *Angew. Chemie - Int. Ed.* **55**, 16039–16043 (2016).
43. Wilhelm, S. *et al.* Analysis of nanoparticle delivery to tumours. *Nat. Rev. Mater.* **1**, 16014 (2016).
44. Von Maltzahn, G. *et al.* Nanoparticle self-assembly gated by logical proteolytic triggers. *J. Am. Chem. Soc.* **129**, 6064–6065 (2007).
45. Badeau, B. A., Comerford, M. P., Arakawa, C. K., Shadish, J. A. & Deforest, C. A. Engineered modular biomaterial logic gates for environmentally triggered therapeutic delivery. *Nat. Chem.* **10**, 251–258 (2018).

Acknowledgements

We thank Dr. H. Fleming (MIT) and Dr. A. Nogiwa-Valdez (Imperial) for critical reading and editing of the manuscript, Dr. M. Kumar (Bioimaging and Chemical Analysis Facilities, MIT) for help with ICP-MS, M. Berne (Tufts University Core Facility) for peptide synthesis, and K. Cormier and Dr. R. Bronson from the Koch Institute Histology Core. We acknowledge use of characterization facilities at the Harvey Flower Electron Microscopy Suite (Department of Materials, Imperial College London) and the Light Microscopy Facilities at the Francis Crick Institute London. This study was supported in part by a Koch Institute Support Grant P30-CA14051 from the National Cancer Institute (Swanson Biotechnology Center), a Core Center Grant P30-ES002109 from the National Institute of Environmental Health Sciences, the Ludwig Fund for Cancer Research, and the Koch Institute Marble Center for Cancer Nanomedicine. C.N.L., Q.C., and M.M.S acknowledge generous support from the i-sense Engineering and Physical Sciences Research Council (EPSRC) IRC in Early Warning Sensing Systems for Infectious Diseases (EP/K031953/1; www.i-sense.org.uk). C.N.L. acknowledges support from the Marshall Aid Commemoration Commission. A.P.S. acknowledges support from the NIH Molecular Biophysics Training Grant and the National Science Foundation Graduate Research Fellowship. J.S.D acknowledges support from the National Science Foundation Graduate Research Fellowship, the Ludwig Center for Molecular Oncology fellowship, and the Siebel Scholar Foundation. A.N. acknowledges support from the Sir Henry Wellcome Postdoctoral Fellowship (209121_Z_17_Z) funding scheme from the Wellcome Trust. S.N.B is a Howard Hughes Medical Institute Investigator. M.M.S., Y.L., and Q.C. acknowledge support from the European Research Council (ERC) Seventh Framework Programme Consolidator grant “Naturale CG” (616417). A.B. acknowledges support from Early Postdoc Fellowship program (P2ELP2_178238) from Swiss National Science Foundation.

Author contributions. C.N.L., A.P.S., J.S.D., S.N.B., and M.M.S. conceived and designed the research. C.N.L. and A.P.S. carried out all experiments and analysed the data. Y.L. assisted with peptide synthesis and characterization, A.N. performed FCS measurements and analysis, A.B. assisted with ICP-MS, and Q.C. assisted with TEM imaging. C.N.L., A.P.S., S.N.B., and M.M.S. wrote the manuscript with feedback from all authors. C.N.L. and A.P.S. contributed equally, and S.N.B. and M.M.S. are joint corresponding authors.

Additional Information

Supplementary information is available in the online version of the paper. Reprints and permission information is available online at www.nature.com/reprints. Correspondence and requests for materials should be addressed to S.N.B. and M.M.S.

Supplementary information

Supplementary Material and Methods, characterization of peptide sequences (LC-MS), characterization of AuNCs and AuNC-NAv complexes (TEM, UV-vis, DLS, catalytic activity assay conditions), stability of AuNCs and AuNC-NAv complexes in physiological environments (FCS, TEM), *in vitro* protease cleavage assays (MMP and thrombin) using gel filtration chromatography, sensitivity of assay for *in vitro* protease detection (FCS and catalytic activity assay), biocompatibility (cell viability, animal weight tracking, histology), pharmacokinetic characterization, organ accumulation of AuNCs and AuNC-NAv complexes in healthy and tumour-bearing mice, and controls for *in vivo* experiments.

Competing financial interests

S.N.B., M.M.S., C.N.L., and A.P.S have filed a patent application related to this research with the US Patent and Trademark Office. S.N.B. is a director at Vertex, co-founder and consultant at Glympse Bio, consultant for Cristal, Maverick, Synlogic, and Moderna, and receives sponsored research funds from Johnson & Johnson and Alnylam Pharmaceuticals.

Abbreviations

AuNC, gold nanocluster; GSH, glutathione; i.v., intravenous; MMP, matrix metalloproteinase; NAv, neutravidin protein; p.i., post injection; PoC, point-of-care; TMB, 3,3',5,5'-Tetramethylbenzidine; THR, thrombin.

Figure Captions

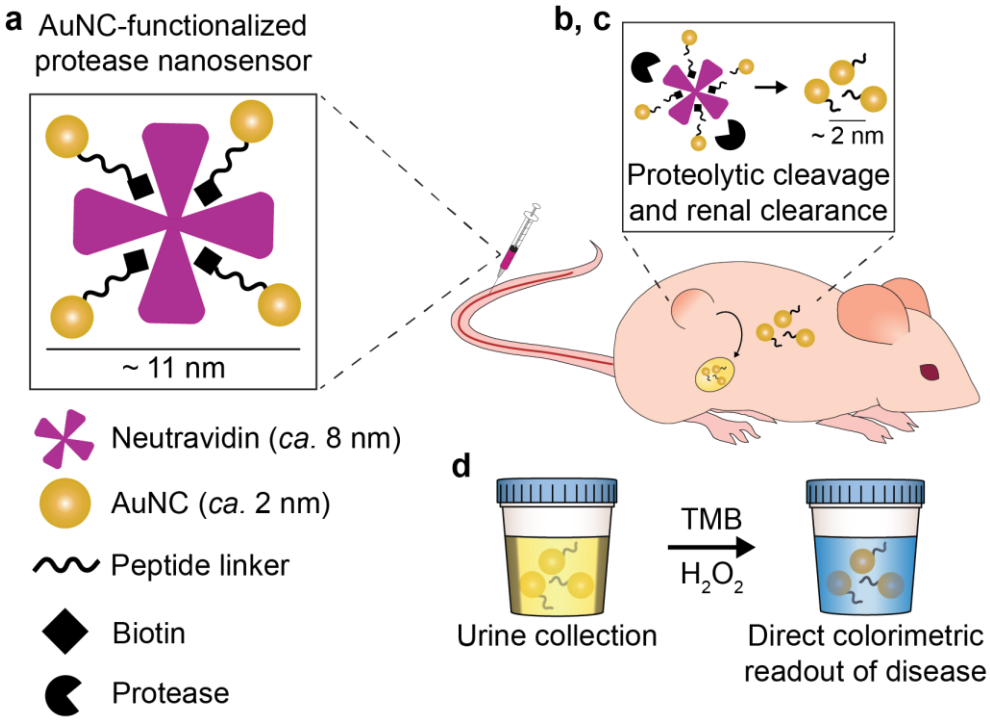

Figure 1. Design of nanocatalyst signal amplification sensing system. (a) Catalytic gold nanoclusters (AuNCs, *ca*. 2 nm) are conjugated to a neutravidin protein scaffold (*ca*. 8 nm) through a biotinylated protease-cleavable peptide linker. (b) The protease-sensitive nanocluster-neutravidin complex (*ca*. 11 nm) is injected intravenously and designed to specifically disassemble when exposed to the activity of relevant dysregulated proteases at the site of disease. (c) After protease cleavage, liberated *ca*. 2 nm AuNCs are filtered into the urine. (d) AuNCs can be detected in cleared urine by measuring their ability to oxidise a chromogenic peroxidase substrate (*e.g*. 3,3′,5,5′-Tetramethylbenzidine, TMB) in the presence of hydrogen peroxide, generating a coloured signal that can be easily read by eye.

Table 1. Protease-cleavable thiol-terminated peptide sequences for AuNC synthesis. Catalytic AuNCs were synthesized using GSH and another thiol-terminated protease-cleavable peptide sequence: $P1_{13}$, $P1_{20}$, $P2_{13}$, or $P2_{20}$, where the subscript indicates the number of amino acid residues in each sequence. AuNCs synthesized with the respective peptides are subsequently labelled AuNC-$P1_{13\text{ or }20}$ and AuNC-$P2_{13\text{ or }20}$.

Substrate ($P_{\#aa}$)	**Protease specificity**	**Sequence (↓ represents scissile bond, enzyme recognition motif bolded)**	**MW (g/mol)**	**Product (g/mol)**
$P1_{13}$	Thrombin	Biotin-SGG**fPR**↓SGGSGGC	1350	846
$P1_{20}$	Thrombin	Biotin-GGGSGGGSGG**fPR**↓SGGGGGC	1750	1275
$P2_{13}$	MMP9	Biotin-GGG**PLG**↓VRGKGGC	1339	683
$P2_{20}$	MMP9	Biotin-GGGGGGGGGG**PLG**↓VRGKGGC	1739	1080

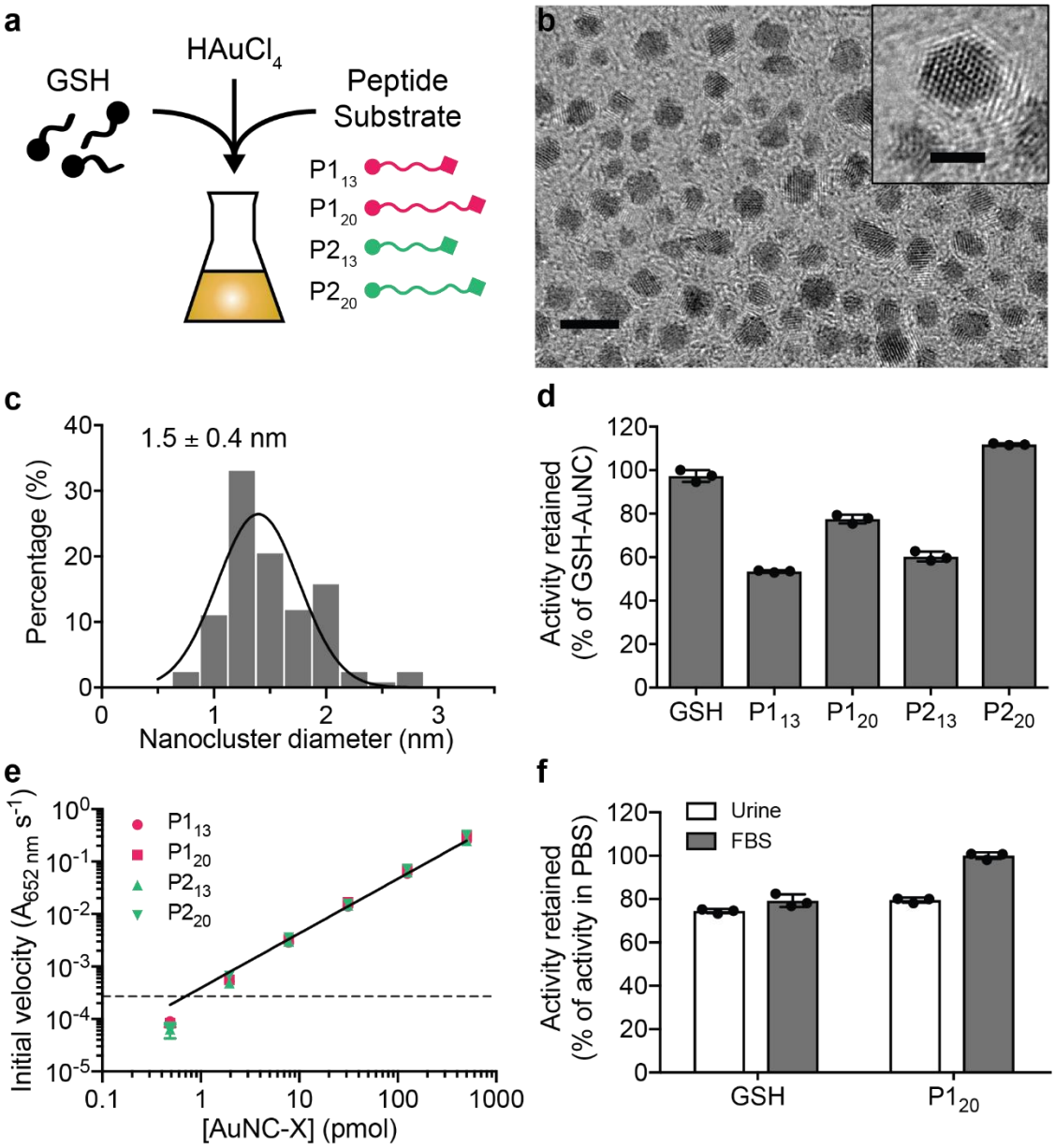

Figure 2. Peptide-functionalised AuNCs exhibit robust catalytic activity. (a) Schematic showing one-pot synthesis of AuNCs where thiol-terminated heterobifunctional peptides ($P1_{13}$, $P1_{20}$, $P2_{13}$, $P2_{20}$) are incorporated onto the AuNC surface. (b) Transmission electron micrograph (TEM) of glutathione-protected AuNCs (GSH-AuNCs, scale = 5 nm). Inset shows high-resolution TEM of an individual GSH-AuNC (scale = 2 nm). (c) Histogram showing results of size analysis from TEM images of GSH-AuNCs (legend shows mean diameter ± s.d., n = 127 particles). Solid line represents Gaussian fit of size distribution. (d) Catalytic activity of AuNCs capped with different cysteine containing protease-cleavable peptide linkers (GSH, $P1_{13}$, $P1_{20}$, $P2_{13}$, $P2_{20}$, Table 1; mean ± s.d., n = 3 independent experiments). Activity was measured by the absorbance at 652 nm corresponding to the oxidation of the chromogenic peroxidase substrate TMB by H_2O_2 and normalized here to the activity of GSH-AuNCs in PBS. (e) Limit of detection of reporter probes in synthetic urine measured by catalytic activity of AuNCs functionalised with peptides, where X = $P1_{13\text{ or }20}$ or $P2_{13\text{ or }20}$ (mean ± s.d., n = 3 independent experiments). Catalytic activity was measured by initial rate analysis ($A_{652\text{ nm}}$ s^{-1}) of TMB oxidation. Solid line indicates activity for AuNCs is linear over 3 orders of magnitude of particle concentration with nonlinear (log scale) regression least-squares fit, R^2 = 0.9996. Dashed line represents limit of detection, which was calculated as 3 standard deviations above the mean background signal. (f) Catalytic activity of GSH-AuNCs and representative AuNC-

$P1_{20}$ batch incubated in urine (undiluted) or serum (undiluted FBS) environments for 1 h. Activity was normalized to activity of AuNCs in PBS (mean ± s.d., *n* = 3 independent experiments).

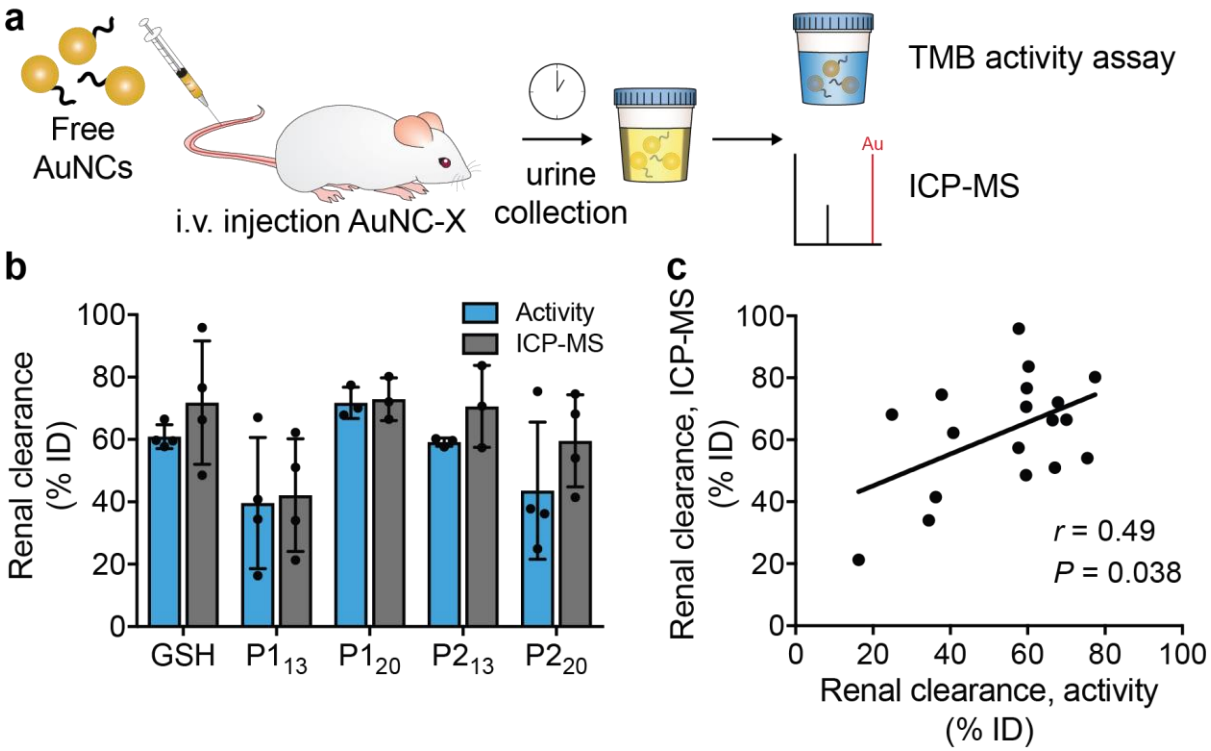

Figure 3. Peptide-functionalised AuNCs clear via the renal system and retain catalytic activity in urine. (a) Schematic of the renal clearance assay. AuNCs were intravenously (i.v.) injected into Swiss Webster mice, and urine was collected 1 h post-injection. Urine was analysed by both TMB catalytic activity assay and by ICP-MS to measure gold content. (b) Renal clearance efficiency of GSH-AuNC, AuNC-$P1_{13}$, AuNC-$P1_{20}$, AuNC-$P2_{13}$, AuNC-$P2_{20}$ as measured by colorimetric assay ($A_{652\ nm}$) and by ICP-MS (estimated ppb cleared), normalized to activity and gold content, respectively, of the injected dose (mean ± s.d., *n* = 3 or 4 mice per group). (c) Correlation between estimated renal clearance as measured by colorimetric activity assay and by ICP-MS (Pearson's *r* = 0.492 with 95% confidence interval 0.0320 to 0.780, *n* = 18 mice, **P* = 0.0383).

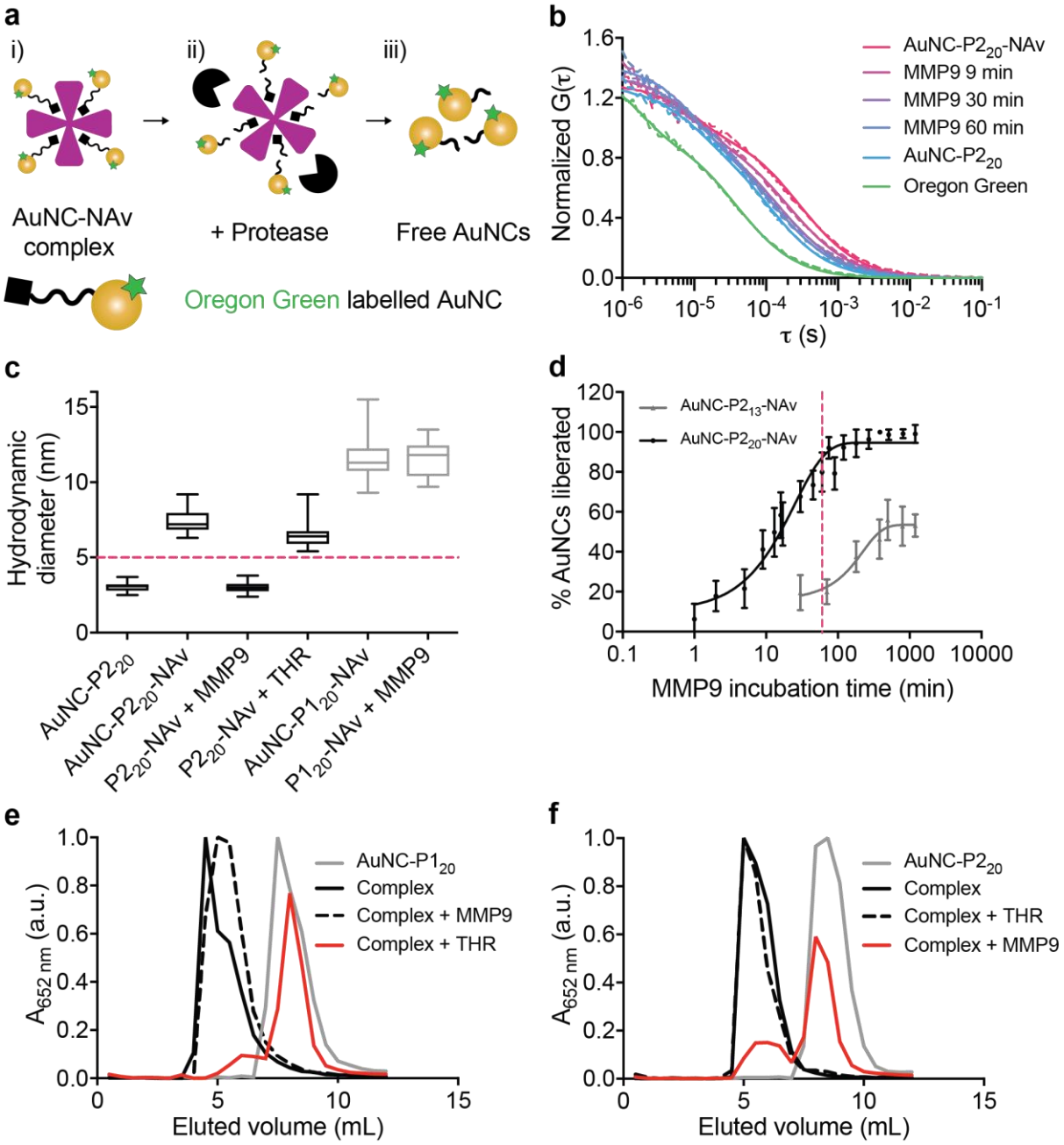

Figure 4. AuNC-neutravidin complexes disassemble *in vitro* in response to protease activity. (a) Schematic illustration of FCS experiment. (i) AuNCs were labelled with a fluorescent dye and complexed to a neutravidin core. (ii) Dye-labelled AuNC-NAv complexes were incubated with the relevant enzyme: MMP9 or thrombin (THR), (iii) and FCS was used to monitor changes in diffusion time due to enzyme cleavage. (b) Average autocorrelation curves from FCS measurements (n = 25 independent measurements) showing AuNC-P2$_{20}$-NAv complex in the presence of MMP9 (50 nM) over time compared to free labelled AuNCs and Oregon Green dye (dashed lines: experimental; solid lines: fits). A clear shift to faster diffusion times was observed for longer enzyme incubation times (red to blue colour change), indicating cleavage of AuNCs from the complex. (c) Hydrodynamic diameters calculated from FCS autocorrelation curves showing changes in sizes of complexes after enzyme incubation: AuNC-P2$_{20}$-NAv + MMP9 (50 nM, 4.5 h) or thrombin (50 nM, 12 h); AuNC-P1$_{20}$-NAv + MMP9 (50 nM, 12 h). Dashed line represents renal filtration size cut-off of *ca*. 5 nm.[32] Center line represents median, box limits represent upper and lower quartiles, and whiskers represent minimum and maximum values (n = 25 independent measurements). (d) Plot of fraction of AuNCs liberated (see FCS in Supplementary Methods) from AuNC-P2$_{13\ or\ 20}$-NAv complex for

MMP-responsive complexes composed of either short or long linker incubated with MMP9 (50 nM) up to 16 h (mean ± s.d., *n* = 25 independent measurements). Dashed line at 60 min corresponds to time frame of *in vivo* experiments. (e) Normalized absorbance measuring catalytic activity of gel filtration chromatography (GFC) column fractions associated with AuNC-$P1_{20}$, thrombin-responsive AuNC-$P1_{20}$-NAv complex (Complex), AuNC-$P1_{20}$-NAv (10 µM) incubated with MMP9 (50 nM, 12 h) (Complex + MMP9), and AuNC-$P1_{20}$-NAv complex (10 µM) incubated with thrombin (50 nM, 12 h) (Complex + THR). (f) Normalized absorbance measuring catalytic activity of GFC column fractions associated with AuNC-$P2_{20}$, MMP-responsive AuNC-$P2_{20}$-NAv complex (Complex), AuNC-$P2_{20}$-NAv complex (10 µM) incubated with thrombin (50 nM, 12 h) (Complex + THR), and AuNC-$P2_{20}$-NAv (10 µM) incubated with MMP9 (50 nM, 12 h) (Complex + MMP9). All enzyme incubations were performed at 37 °C and all GFC experiments were repeated independently 3 times with similar results.

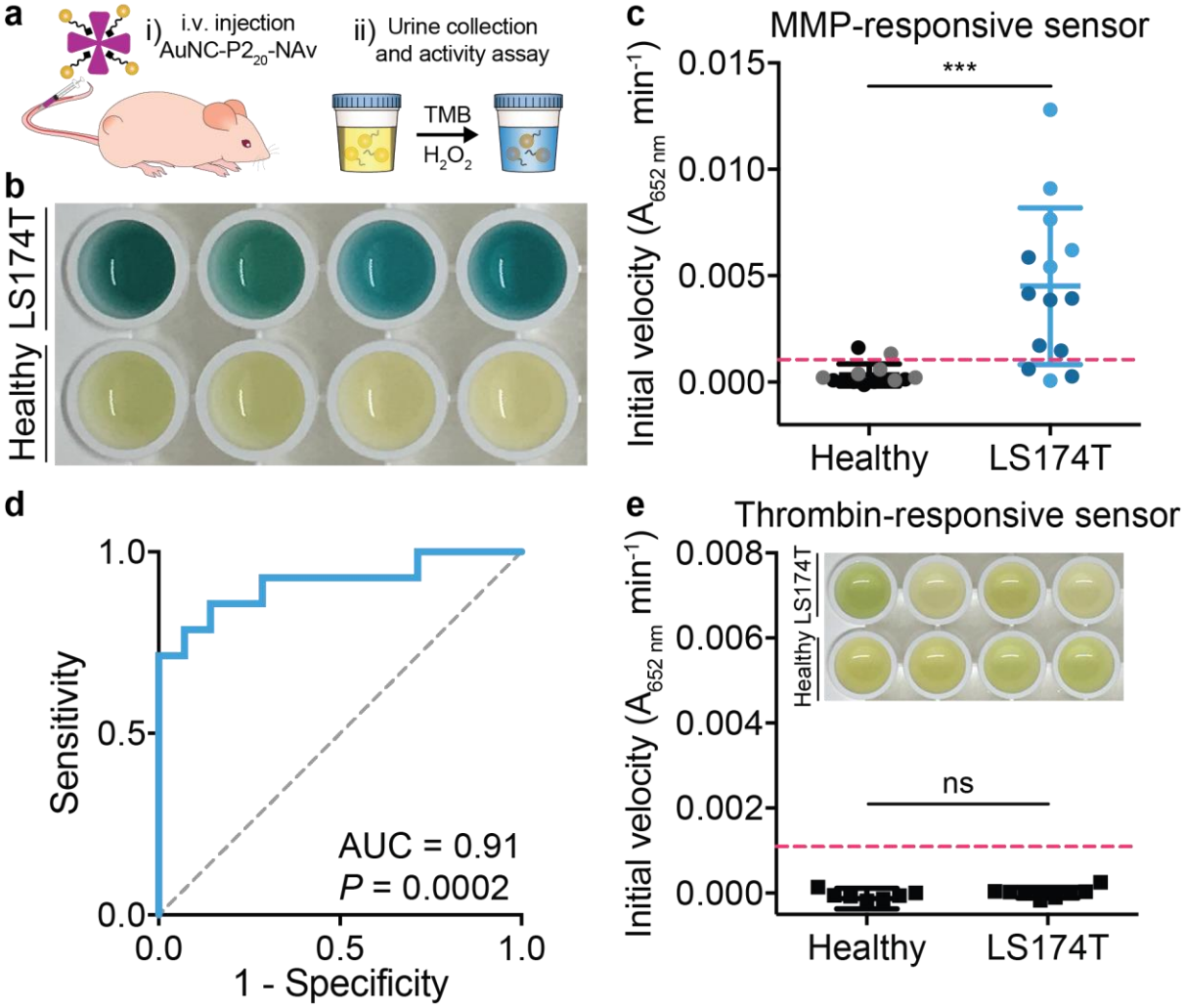

Figure 5. AuNC-functionalised protease nanosensors enable direct colorimetric urinary readout of disease state. (a) (i) Mice bearing LS174T flank xenografts (2 weeks post inoculation) and age-matched healthy controls were injected intravenously with AuNC-$P2_{20}$-NAv complex. (ii) Urine was collected 1 h p.i., and renal clearance of liberated AuNCs was measured by catalytic activity assay. (b) Photograph of representative examples of colorimetric assay on urine from tumour-bearing (top) and healthy (bottom) mice injected with AuNC-$P2_{20}$-NAv (*n* = 4 mice per group shown). (c) Catalytic activity assay on urine collected from healthy and LS174T tumour-bearing mice 1 h after injection with AuNC-$P2_{20}$-NAv complex (mean ± s.d., *N* = 2 independent experiments indicated in shades, *n* = 6 (gray and light blue) or 8 (black and dark blue) mice per group, two-tailed Mann-Whitney test, ****P* = 0.0002). Catalytic activity is measured by initial rate analysis ($A_{652\,nm}$ min^{-1}), and dashed line

represents limit of detection (see Methods). (d) Receiver-operating characteristic (ROC) curve by initial velocity of catalytic activity assay discriminated healthy from diseased mice with an AUC of 0.91 (*N* = 2 independent experiments, *n* = 6 or 8 mice per group as in Fig. 5c, *P* = 0.0002 from random classifier shown in dashed line). (e) Catalytic activity assay on urine from healthy and tumour-bearing mice injected with thrombin-responsive AuNC-$P1_{20}$-NAv complex. Inset: photograph of representative examples. No visible colorimetric development was observed in either group, and there was no statistically significant difference between the two groups (mean ± s.d., *n* = 8 mice per group, two-tailed Mann-Whitney test, ^{ns}P = 0.161). - Catalytic activity is measured by initial rate analysis ($A_{652\ nm}$ min^{-1}), and dashed line represents limit of detection (see Methods).

METHODS

Materials

All chemicals were purchased from Sigma-Aldrich unless otherwise stated. Milli-Q water (18.2 MΩ.cm) was used in all the experiments.

AuNC synthesis

Synthesis and purification of peptide capped AuNCs followed published procedures with modifications outlined below.[1] We varied the ratio of protease-cleavable peptide substrate to glutathione in the AuNC synthesis to incorporate functional handles onto the AuNC surface (P1:GSH or P2:GSH, tested at 1:2, 1:4, 1:5, 1:9). Briefly, freshly prepared aqueous solution of gold(III) chloride trihydrate aqueous solution ($HAuCl_4$, 20 mM, 100 µL) was mixed with 750 µL deionized water in an Eppendorf tube, followed by fast addition of L-Glutathione reduced (GSH, 20 mM) and either peptide P1 or P2 (20 mM) so that final peptide content was fixed at a total volume of 150 µL in varying ratios of P1 or P2:GSH at 25 °C. The reaction mixture was heated to 70 °C under gentle stirring (500 rpm) for 24 h. The reaction mixture changed from yellow to colourless within minutes and then turned pale yellow over *ca*. 12 h, indicating first reduction of Au (III) to Au (I) by the thiol group of the peptides, followed by the reduction of Au(I) thiolate complexes to Au(0) atoms over time assisted by the favourable reduction kinetics at the elevated reaction temperature.[2,3] After 24 h synthesis, the resulting AuNC solution exhibited both orange luminescence and simultaneous peroxidase-like activity. The AuNCs could be stored at 4 °C for > 6 months with negligible changes in optical or catalytic properties. The as-prepared AuNCs were purified through centrifugal ultrafiltration (Amicon Ultra centrifugal filter units Ultra-15, MWCO 10 kDa, Sigma) and buffer exchanged into phosphate buffered saline (PBS, pH 7.2). During ultrafiltration, the AuNCs were collected in the concentrate in the filter device, while any unbound peptide was collected in the filtrate. After purification, AuNCs were resuspended in PBS (20 µM by AuNC particle concentration) and sterile filtered (Millex-GV Filter, Millipore, 0.22 µm).

The number of biotinylated ligands per AuNC was calculated by measuring biotin concentration in the filtrate from AuNC purification above, and subsequently subtracting this value from the starting concentration of biotinylated peptide in the synthesis. Biotin concentration in the filtrate was quantified using the Pierce Biotin Quantitation kit in a 96-well plate following manufacturer's instructions (Thermo Fisher) without any modifications. The molarity of biotin in the sample was calculated using the extinction coefficient for HABA/avidin at 500 nm of 34,000 $M^{-1}cm^{-1}$ and path length of 0.5 cm.

Characterization of nanoparticles

Dynamic light scattering (DLS, Zeta Sizer Nanoseries, Malvern Instruments, Ltd.) was used to characterize the hydrodynamic diameter of nanoparticles. Absorption measurements were recorded on a SpectraMax M5 multimode microplate reader (Molecular Devices, Ltd.). For electron microscopy characterization, samples were drop-casted onto carbon-coated copper grids (Electron Microscopy Sciences), and TEM imaging was performed using a JEOL 2100F operating at 200 kV. For preparation of TEM samples, AuNC samples were first desalted (Zeba Spin Desalting Columns, 7K MWCO, Sigma) and 5 µL desalted sample was dropped onto the grid, allowed to incubate for 5 min, and subsequently wicked with filter paper and dried overnight before imaging.

Evaluation of peroxidase-like activity

The colorimetric readout was carefully optimized to maximize signal intensity from AuNCs by varying the concentration of hydrogen peroxide, pH, and concentration of sodium chloride, and measuring corresponding catalytic activity under these conditions (Supplementary Fig. 6**,** Supplementary Table 2). For stability and catalytic activity of AuNCs in physiological environments, AuNCs (20 µM, 50 µL) were incubated with PBS (50 µL), synthetic urine (Surine Negative Urine Control, Sigma), or fetal bovine serum (FBS, Gibco) for 1 h at 37 °C followed by five-fold dilution in water. For the activity assay, 50 uL of each sample was added to a 96-well plate (Corning, UK) followed by 150 uL chromogenic substrate solution: 1-Step Ultra TMB ELISA Substrate Solution (Thermo Scientific) spiked to a final concentration of 4 M hydrogen peroxide (30% (w/w), Sigma). The absorbance of the reaction solution at 652 nm was monitored up to 25 min after addition of substrate, corresponding to oxidation of TMB by H_2O_2.

For limit of detection (LOD) assays, in a 96-well plate, synthetic urine (25 µL) was mixed with AuNCs (25 µL, varying concentrations, diluted in PBS), 5 M H_2O_2 (100 µL), and 1-Step Ultra TMB ELISA Substrate Solution (100 µL). Absorbance at 652 nm was measured every 20 s for 10 min, and linear regression was used to calculate the slope ($A_{652\ nm}\ s^{-1}$) over the first 150 sec. LOD was calculated as 3 standard deviations above the mean background signal.

AuNC-NAv complex assembly

In a typical conjugation, 125 µL NeutrAvidin Protein (120 µM, PBS, Thermo Fisher, NAv) was mixed with 1 mL of AuNC-P1 or AuNC-P2 (20 µM) and incubated for 12 h gently shaking (500 rpm) at 37 °C. Unbound AuNCs were removed from AuNC-NAv complexes through centrifugal ultrafiltration (Amicon Ultra centrifugal filter units Ultra-15, MWCO 50 kDa, Sigma), where AuNC-NAv complexes remained in concentrate and any unbound AuNCs were collected in

the filtrate. After ultrafiltration, AuNC-NAv complexes were resuspended in PBS (30 µM by [AuNC]) and sterile filtered (Millex-GV Filter, Millipore, 0.22 µm).

In vivo renal clearance studies

All animal studies were approved by the Massachusetts Institute of Technology (MIT) committee on animal care (MIT protocol 0417-025-20). All animals received humane care, and all experiments were conducted in compliance with institutional and national guidelines. GSH-templated and substrate functionalised AuNCs were diluted to 10 µM [AuNC] in sterile PBS. Female Swiss Webster mice (4-6 weeks old, Taconic) were intravenously administered 2000 pmol AuNCs via the tail vein (10 µM [AuNC], 200 µL). The injected dose of glutathione-templated gold nanoclusters ranged from 1.6 to 2.4 mg kg^{-1} in terms of gold content, which is well below the maximal tolerated dose reported for both mice and non-human primates (1059 mg kg^{-1} by particle concentration, ~530 mg kg^{-1} by gold content).[4]

After nanocluster injection, urine was collected at the indicated timepoints for catalytic activity assay and ICP-MS measurements. Mice were placed in custom housing with a 96-well plate base for urine collection. After 1 h, their bladders were voided, and collected urine volume was measured. Clearance of active AuNCs was quantified via catalytic activity assay, and urine gold content was quantified by ICP-MS. Pearson's correlation coefficient (*r*) was computed to assess the relationship between renal clearance as measured by catalytic activity assay or ICP-MS (gold content).

Urine catalytic activity assays

For all assays, 25 µL of urine was diluted into 25 µL PBS in a transparent 96-well plate and allowed to equilibrate at room temperature for 15 min. 100 µL each of 5 M H_2O_2 (Sigma) and TMB (ThermoFisher Scientific) were then added, and the plate was read kinetically at 652 nm over the course of 30 min. In all catalytic activity assays involving AuNCs in collected urine, the final pH is acidic due to the acidic pH of the TMB and hydrogen peroxide substrate mix resulting in a final reaction pH < 4. For renal clearance studies, the concentration of active AuNCs present in the urine was quantified via reference to a calibration curve of known AuNC concentrations. For disease detection studies, the initial reaction velocity was quantified as the rate of change of the absorbance at 652 nm over the first 10 min of the reaction (A_{652} min^{-1}). Initial velocity analysis was preferred over analysis of a single time point measurement of absorbance at 652 nm, as urine collected from different mice had varying degrees of background levels of absorbance at this wavelength based on the hydration state of each mouse. This variable background was removed in the initial velocity analysis as the background absorbance from initial coloration of urine was constant over time. Limit of

detection was calculated to be the lowest concentration of the linear portion of the calibration curve (measured as the initial rate of catalytic activity of relevant AuNC batch).

Inductively coupled plasma-mass spectrometry (ICP-MS) on urine samples

Urine samples were digested in aqua regia for 24 h. The digested samples were further diluted in an ICP-MS matrix composed of 4% HCl / 4% HNO_3. The gold content in each sample was measured using an Agilent 7900 ICP-MS using an indium internal standard (5 ppb) and gold standard (TraceCERT, Sigma) for the calibration curve prepared in the ICP-MS matrix.

Cell culture

For xenograft studies, LS174T (ATCC CL-188) cells were cultured in Eagle's Minimal Essential Medium (EMEM, ATCC) supplemented with 10% (v/v) FBS (Gibco) and 1% (v/v) penicillin-streptomycin (CellGro). For *in vitro* cytotoxicity assays, HEK293T (ATCC CRL-3216) cells were cultured in Dulbecco's Modified Eagle Medium (DMEM, ATCC) supplemented with 10% (v/v) FBS (Gibco) and 1% (v/v) penicillin-streptomycin (CellGro). Cells were passaged when confluence reached 80%.

***In vitro* cytotoxicity studies**

For *in vitro* cytotoxicity studies, HEK293T cells were plated in a 96-well plate (10,000 cells per well) and allowed to adhere to the wells. 24 h post seeding, cells were incubated with varying concentrations of AuNC-NAv complex (diluted in PBS) for 24 h. Cell viability was evaluated using the MTS (3-(4,5-dimethylthiazol-2-yl)-5-(3-carboxymethoxyphenyl)-2-(4-sulfophenyl)-2H-tetrazolium) assay (Promega).

***In vivo* toxicity studies**

AuNC-NAv complex (AuNC-$P1_{20}$-NAv or AuNC-$P2_{20}$-NAv, 15 µM [AuNC], 200 µL ~ 3000 pmol) was intravenously injected into immunocompetent female Swiss Webster mice (4-6 weeks old, Taconic). The mass of each mouse was monitored for 4 weeks p.i. and compared with masses of PBS injected control mice. Heart, lung, liver, spleen, and kidney tissues were collected from the mice at 1 h, 24 h, or 10 days p.i., fixed in 10 wt% formalin, paraffin embedded, stained with haematoxylin and eosin, and then examined by a veterinary pathologist and compared to organs from PBS injected control mice.

Pharmacokinetic studies

To analyse the blood half-life of the AuNC-NAv complex, female Swiss Webster mice (4-6 weeks old, Taconic) were injected with AuNC-$P2_{20}$-NAv (15 µM [AuNC], 200 µL ~ 3000 pmol) labelled with the photostable near-IR dye Alexa Fluor 750 Succinimidyl Ester (Invitrogen).

Blood was withdrawn retro-orbitally (~70 µL) and then immediately transferred into 70 µL of PBS with 5 mM EDTA and centrifuged to pellet blood cells. Concentration of the AuNC-NAv complex in plasma was measured using an Odyssey infrared scanner (Li-Cor Inc.).

For biodistribution studies in healthy animals, female Swiss Webster mice (4-6 weeks old, Taconic) were injected with either IR-dye labelled AuNCs (10 µM [AuNC], 200 µL ~ 2000 pmol) or AuNC-$P2_{20}$-NAv (15 µM [AuNC], 200 µL ~ 3000 pmol) complexes. Mice were sacrificed at 1 h, 3 h, 24 h, 1 week, or 4 weeks p.i., and organ and tumour accumulation was measured using an Odyssey scanner and quantified using ImageStudio (Version 5.2, Li-Cor Inc.). Organ accumulation was quantified as signal intensity per unit area, calculated for each organ as the difference between the experimental group (near IR-dye labelled AuNCs or AuNC-$P2_{20}$-NAv) versus the PBS-injected control. Values were scaled by a constant factor for all time points within each treatment group (near IR-dye labelled AuNCs or AuNC-$P2_{20}$-NAv) to fall within the range shown. For mice injected with free AuNCs, urine was also collected at the indicated time points and analysed by both ICP-MS (for gold content analysis) and catalytic activity assay.

For biodistribution studies in tumour-bearing mice, nude mice bearing LS174T flank tumours were infused with either near IR-dye labelled neutravidin carrier (VivoTag750, PerkinElmer; 1 µM by VT750), MMP-cleavable AuNC-$P2_{20}$-NAv complex (15 µM [AuNC], 200 µL ~ 3000 pmol, Alexa Fluor 750), or free AuNCs (10 µM [AuNC], 200 µL ~ 2000 pmol, Alexa Fluor 750). Mice were sacrificed 1 h p.i., and organ and tumour accumulation was measured using an Odyssey scanner and quantified using ImageStudio (Version 5.2, Li-Cor Inc.). Organ accumulation was quantified as signal intensity per unit area, calculated for each organ as the difference between the experimental group (fluorescently labelled carrier, complex, or free nanocluster) versus the PBS-injected control, and scaled to fall within the range shown.

Colorectal cancer xenograft studies

Female NCr Nude mice (4-5 weeks, Taconic) were injected bilaterally with 3 x 10^6 LS174T cells per flank. Two weeks after inoculation, tumour-bearing mice and age-matched controls were injected with either 15 µM MMP-sensitive or thrombin-sensitive (control) AuNC nanosensors in 200 µL of PBS (concentrations determined by [AuNC]). After nanosensor injection, mice were placed in custom housing with a 96-well plate base for urine collection. Based on the measured blood half-life of the AuNC-NAv complex, the degree of tumour accumulation 1 h p.i., as well as our results from the FCS cleavage assays (80% of AuNCs cleaved from complex within 1 h), we selected 1 h p.i. as our time point for urine collection.[5–7] After 1 h, bladders of the mice were voided to collect between 100-200 µL of urine. Urine was

analysed via the catalytic activity measurements described above.

Statistical analyses

All statistical analyses were conducted in GraphPad 7.0 (Prism). All sample sizes and statistical tests are specified in figure legends. The D'Agostino-Pearson test was used to assess normality and thus determined the statistical test used. For each animal experiment, groups were established before tumorigenesis or treatment with AuNC-PX, and therefore no randomization was used in the allocation of groups. Investigators were not blinded to the groups and treatments during the experiments.

Data Availability

Research data is available online at DOI:10.5281/zenodo.3256265.

References (Methods section)

1. Zhang, X.-D. *et al.* Ultrasmall glutathione-protected gold nanoclusters as next generation radiotherapy sensitizers with high tumor uptake and high renal clearance. *Sci. Rep.* **5**, 8669 (2015).
2. Yu, Y., Luo, Z., Yu, Y., Lee, J. Y. & Xie, J. Observation of cluster size growth in CO-directed synthesis of Au 25(SR) 18 nanoclusters. *ACS Nano* **6**, 7920–7927 (2012).
3. Luo, Z. *et al.* From aggregation-induced emission of Au(I)-thiolate complexes to ultrabright Au(0)@Au(I)-thiolate core-shell nanoclusters. *J. Am. Chem. Soc.* **134**, 16662–16670 (2012).
4. Xu, J. *et al.* Dose Dependencies and Biocompatibility of Renal Clearable Gold Nanoparticles: From Mice to Non-human Primates. *Angew. Chemie - Int. Ed.* **57**, 266–271 (2018).
5. Kwong, G. A. *et al.* Mass-encoded synthetic biomarkers for multiplexed urinary monitoring of disease. *Nat. Biotechnol.* **31**, 63–70 (2013).
6. Warren, A. D., Kwong, G. A., Wood, D. K., Lin, K. Y. & Bhatia, S. N. Point-of-care diagnostics for noncommunicable diseases using synthetic urinary biomarkers and paper microfluidics. *Proc. Natl. Acad. Sci. U. S. A.* **111**, 3671–6 (2014).
7. Kwon, E. J., Dudani, J. S. & Bhatia, S. N. Ultrasensitive tumour-penetrating nanosensors of protease activity. *Nat. Biomed. Eng.* **1**, 0054 (2017).

Renal clearable catalytic gold nanoclusters for *in vivo* disease monitoring

Colleen N. Loynachan†, Ava P. Soleimany†, Jaideep S. Dudani, Yiyang Lin, Adrian Najer, Ahmet Bekdemir, Qu Chen, Sangeeta N. Bhatia*, Molly M. Stevens*

†***Contributed equally*; *co-corresponding authors***

Supplementary Materials and Methods

Solid phase peptide synthesis

Peptides were synthesized manually on Rink amide resin using standard fluorenyl methoxycarbonyl (Fmoc) chemistry. The Fmoc protecting group was removed from the resin by incubating with piperidine/DMF (20:80) for 2 x 10 min. Fmoc-protected amino acids were activated with 4 molar equivalents of the Fmoc protected amino acids, 3.95 molar equivalents of *N,N,N′,N′* -Tetramethyl-*O*-(1*H*-benzotriazol-1-yl)uronium hexafluorophosphate, and 6 molar equivalents of diisopropylethylamine in DMF. The coupling solution was added to the resin and the coupling reaction was allowed to proceed for 3 h. Peptides were cleaved in trifluoroacetic acid/triisopropylsilane/H_2O (95:2.5:2.5) containing DTT for 4 h. The solvent was removed in vacuum and the peptide was precipitated in cold ether. The crude products were further purified using reversed phase preparative high-performance liquid chromatography (Shimadzu) in an acetonitrile/water gradient under acidic conditions on a Phenomenex C18 Gemini NX column (5 micron pore size, a 110 Å particle size, 150 x 21.2 mm). Molecular weight of peptides was verified using liquid chromatography-mass spectrometry (LC-MS, Agilent Technologies).

In vitro gel filtration chromatography assays

AuNC-NAv complexes (10 µM) were first incubated with a recombinant enzyme: MMP9 (Active, Human, Recombinant, PF140, Merck Millipore); MMP7 (Active, Human, Recombinant, *E. coli*, 444270, Merck Millipore); MMP13 (Active, Human, Recombinant, 444287); or thrombin from human plasma (T7009, Sigma, 100 $U \cdot mL^{-1}$ in a 0.1% (w/v) bovine serum albumin solution). Enzyme and AuNC-NAv were incubated at 37 °C gently shaking (500 rpm). Incubation times varied (1 – 12 h) and concentration of enzyme was fixed at 50 nM, where the final peptide substrate concentration was maintained at > 1000 molar excess to enzyme concentration.

Three identical glass chromatography columns were packed with Sephacryl S200 high resolution resin (column D: 1 cm, H: 18 cm, resin: GE Healthcare Life Sciences, fractionation range for globular proteins 5– 250 kDa) to separate samples based on size. Columns were thoroughly cleaned between experiments with PBS. In a typical GFC experiment, *ca*. 200 µL of 10 µM AuNC-PX, AuNC-PX-NAv, and AuNC-PX-NAv

+ 50 nM enzyme (after incubation) were loaded onto each column in parallel. As soon as the sample was added to the resin bed, 24, 500 µL fractions were collected into individual Eppendorf tubes, while PBS was added to the column reservoir. After fractions were collected, a catalytic activity assay was performed on the samples. For the activity assay, 100 µL of each fraction was added to a 96-well plate, followed by 100 µL substrate solution (1-Step Ultra TMB ELISA Substrate Solution with 4 M H_2O_2). The absorbance of the reaction solution at 652 nm was monitored up to 30 min after addition of substrate, corresponding to oxidation of TMB by H_2O_2. The composition of the sample could be determined based on how quickly it eluted from the column as measured by activity. Larger AuNC-NAv complexes elute within the first 7 mL, and smaller bare AuNCs elute more slowly and are found in 7 – 12 mL, corroborated by DLS of column fractions. Absorbance at a fixed time point was plotted as a function of eluted volume, where clear peaks in absorbance are associated with either AuNC-NAv complexes or bare AuNCs. For AuNC-NAv complexes incubated with enzymes, the proportion of liberated AuNCs could be measured by calculating the area under the curve corresponding to 7-12 mL eluted volume (fractions corresponding to bare AuNCs).

Fluorescence correlation spectroscopy

FCS is an autocorrelation analysis of temporal fluctuations of fluorescence intensity due to diffusion of fluorescent particles in and out of a small observation volume, useful for monitoring binding or cleavage events by analysing changes in diffusivity over time. For FCS analysis, AuNC batches were labelled with Oregon Green fluorescent dye (at the free amino group of GSH) and assembled into complexes with the neutravidin core. AuNC-P1 and AuNC-P2 were labelled with 50 molar excess reactive dye (Oregon Green 488 Carboxylic Acid, Succinimidyl Ester, 6-isomer, Thermo Fisher), further called AuNC-PX-OG. Unreacted dye was removed using Zeba Spin Desalting Columns 7K MWCO (Thermo Fisher). AuNC-PX-OG-NAv complexes were assembled following above protocol and purified to remove unbound AuNC-PX-OG. AuNC-PX-OG-NAv complexes were further incubated with enzymes, and kinetics of AuNC-NAv complex disassembly via substrate cleavage was monitored over time using FCS.

Sample preparation for measuring enzyme cleavage kinetics

For MMP9: 0.33 µL MMP9 stock (Merck PF140 lot#2872521, 0.1 mg·mL^{-1} ~ 1500 nM, 57.28 Units/h/µg P) was added per 10 µL sample stock (20 µM, AuNC), for a final enzyme concentration of 50 nM, with AuNCs in 400 molar excess to MMP9. Since AuNCs bear *ca*. 20 peptide substrates per particle, there was *ca*. 8000 molar excess peptide substrates per enzyme. **For thrombin**: 0.58 µL thrombin stock (100 U·mL^{-1}, 32 µg·mL^{-1} ~ 860 nM) was added per 10 µL sample stock (20 µM, AuNC), for a final enzyme concentration of 50 nM, with AuNCs in 400 molar excess to thrombin. All enzyme incubations were performed at 37 °C, and incubations longer than 3 h were maintained at 37 °C while shaking (300 rpm). Samples were then diluted in pre-warmed PBS for FCS measurements.

FCS measurements

In the measurement, labelled particles diffuse through the detection volume, producing a fluctuating fluorescence signal which is subjected to an autocorrelation algorithm yielding an autocorrelation curve, $G(\tau)$, which shows the mobility of the particles. The diffusion time of the particles, τ_D, can be estimated from the inflection of the decay of the autocorrelation curve.

FCS was performed on a commercial LSM 880 (Carl Zeiss, Jena, Germany) equipped with an incubation chamber. All measurements were performed at 37 °C. An Ar^+ laser was used as excitation source for the 488 nm wavelength. Appropriate filter sets were used to detect the fluorescence signal (LP 505). The laser beam passed through a 40x C-Apochromat water immersion objective with a numeric aperture of 1.2 to focus the beam into the sample droplet. Measurements were performed 200 µm above the ibidi 8-well bottom plate (80826, ibidi, Germany) using a 5 µL droplet of sample for each condition. OregonGreen 488 carboxylic acid in PBS (OG488, O6149, ThermoFisher Scientific, NHS-ester was first deactivated by overnight incubation in PBS at room temperature) was used as a standard to calibrate the beam waist (D = 4.1 x 10^{-6} cm^2/s at 25 °C, and when corrected for the higher temperature used: D = 5.49 x 10^{-6} cm^2/s at 37 °C).[1] Immediately before the measurement, stocks or incubated samples were diluted 100-fold in pre-warmed PBS and 5 µL was placed into the measuring chamber. The sample was equilibrated and bleached for 5 x 5 s and 25 x 5 s intensity traces were recorded, autocorrelated and analysed for each sample. Autocorrelation curves were created in ZEN software (Carl Zeiss, Jena, Germany) and

the curves were exported for further analysis using PyCorrfit program 1.1.1.[2] For all the graphs, data for the 25 curves are given except for the autocorrelation curves, which are always the average curve for the whole measurement (125 s).To calculate the percentage of AuNCs cleaved from the AuNC-NAv complex, stocks of clusters/complexes were first fitted using one component fits ($G_{1comp}(\tau)$) to obtain the diffusion times for the pure components. Second, samples incubated with enzymes were fitted with two component fits ($G_{2comp}(\tau)$) with one component fixed to pure cluster diffusion (τ_1) and the other fixed to pure complex diffusion (τ_2) to yield the fraction of free clusters (F_1), which is equivalent to the fraction cleaved. A triplet fraction with a triplet time of 10 µs was included for all the curves.

$$Equation\ 1: G_{1comp}(\tau) = \left(1 + \frac{T}{1-T} e^{\frac{-\tau}{\tau_{trip}}}\right) * \frac{1}{N * \left(1 + \frac{\tau}{\tau_D}\right) * \sqrt{1 + \frac{\tau}{SP^2 \tau_D}}}$$

$$Equation\ 2: G_{2comp}$$
$$= \left(1 + \frac{T}{1-T} e^{\frac{-\tau}{\tau_{trip}}}\right) * \frac{1}{N}$$
$$* \left[\frac{F_1}{\left(1 + \frac{\tau}{\tau_1}\right) * \sqrt{1 + \frac{\tau}{SP^2 \tau_1}}} + \frac{1 - F_1}{\left(1 + \frac{\tau}{\tau_2}\right) * \sqrt{1 + \frac{\tau}{SP^2 \tau_2}}}\right]$$

T is the triplet fraction with corresponding triplet time τ_{trip}, N is the effective number of diffusing species in the confocal volume ($N = n1 + n2$), τ_D is the diffusion time (τ_1, τ_2 diffusion times of corresponding fractions), F_1 fraction of component with diffusion time τ_1, and SP is the structural parameter describing the ratio of height to width of the confocal volume (fixed to 5). The following equation relates the x-y dimension of the confocal volume (ω_{xy}^2), which was calibrated by a standard measurement of OG488 in PBS, to the diffusion coefficient (D), which was calculated for each sample using the obtained diffusion time (τ_D):

$$Equation\ 3: D = \frac{\omega_{xy}^2}{4\tau_D}$$

Stokes-Einstein equation was used to calculate hydrodynamic diameter via the obtained diffusion coefficients. For the AuNC-$P2_{13}$-NAv complex, the percentage of cleaved AuNCs with time was linear over the first 500 minutes of MMP9 incubation, whereas for AuNC-$P2_{20}$-NAv the percentage cleaved was linear over just the first 16 min. of enzyme incubation. The linear regions were analysed by linear regression, and the rates of cleavage were calculated.

In vitro cleavage assays with quenched substrates

P1Q (1 μM by peptide) was incubated with recombinant mouse thrombin (12.5 nM working concentration; Haematologic Technologies) in a 384-well plate at 37°C in PBS-BSA (0.1% w/v). P2Q (1 μM by peptide) was incubated with recombinant human MMP-9 (100 nM working concentration; Enzo Life Sciences) in activity buffer (50 mM Tris, 150 mM NaCl, 5 mM $CaCl_2$, 1 μM $ZnCl_2$) containing 0.1 wt% BSA. Fluorescence dequenching was monitored at 37 °C using a Tecan Infinite microplate reader.

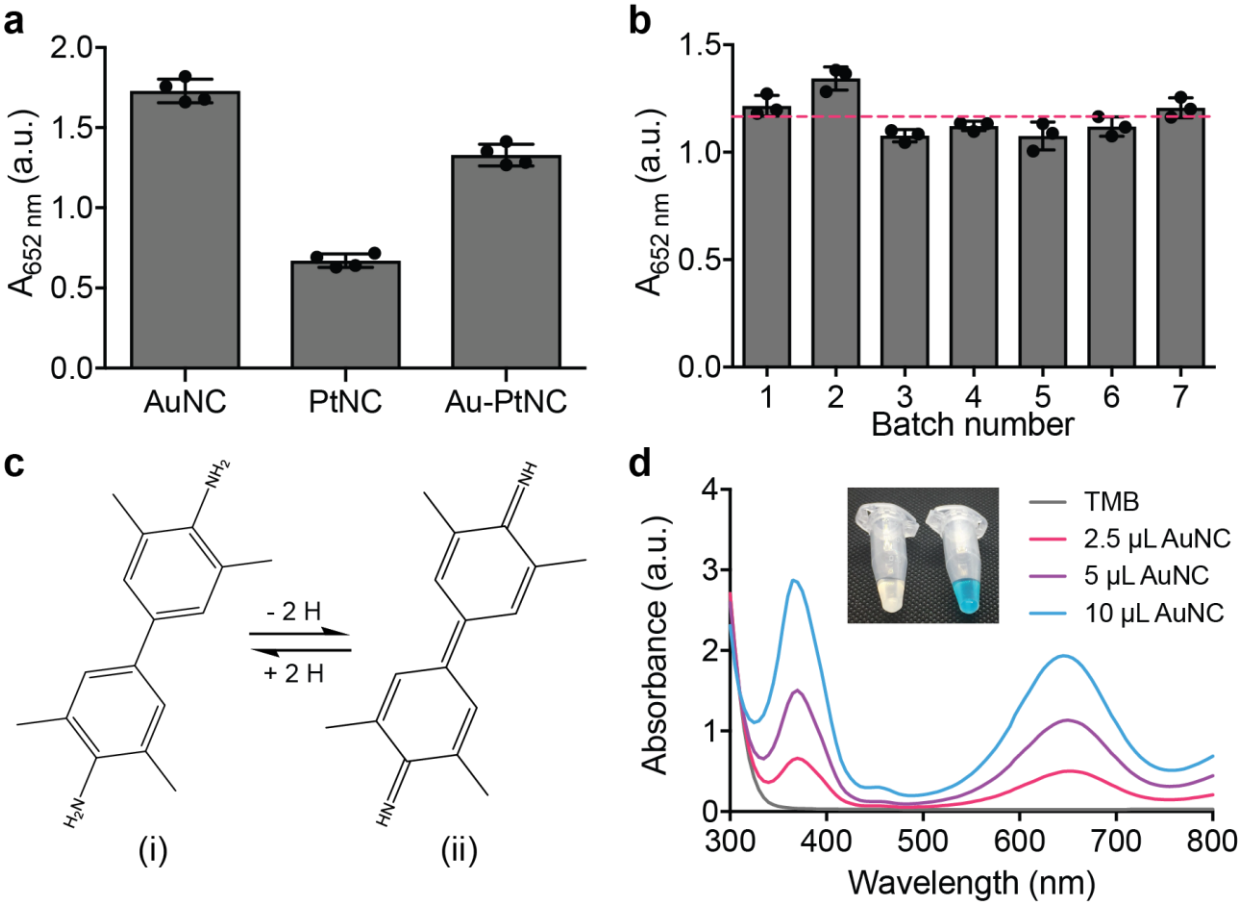

Supplementary Figure 1. Synthesis of peptide-templated nanoclusters. (a) Catalytic activity of glutathione-templated nanoclusters synthesized with varying core metals: gold, platinum, and gold-platinum bimetallic hybrid. AuNCs exhibited the highest activity followed by Au-Pt with intermediate activity, and PtNCs showed the lowest activity of the tested metals when synthesized with a fixed GSH:[Metal] of 1.5 (mean ± s.d., *n* = 4 independent experiments). (b) AuNC synthesis showed high reproducibility in terms of catalytic activity with a coefficient of variation between 7 independently synthesized batches of 8.5 % (mean ± s.d., *n* = 3 independent experiments). The red line indicates the average catalytic activity measured as absorbance at 652 nm corresponding to the oxidation of TMB across 7 AuNC batches. (c) Structure of 3,3',5,5'-tetramethybenzidine (TMB) (i), and oxidised TMB (TMB diimine) (ii). (d) Representative UV/vis spectra showing increase in absorbance correlated to oxidation of TMB in presence of varying concentrations of AuNCs, where the experiment was repeated independently 3 times with similar results. An increase in absorbance at both 370 nm and 652 nm was observed for increasing concentration of nanocatalyst with fixed concentrations of TMB and H_2O_2 substrates. Inset shows photo of substrate alone (left) and substrate with AuNCs with blue colour development (right).

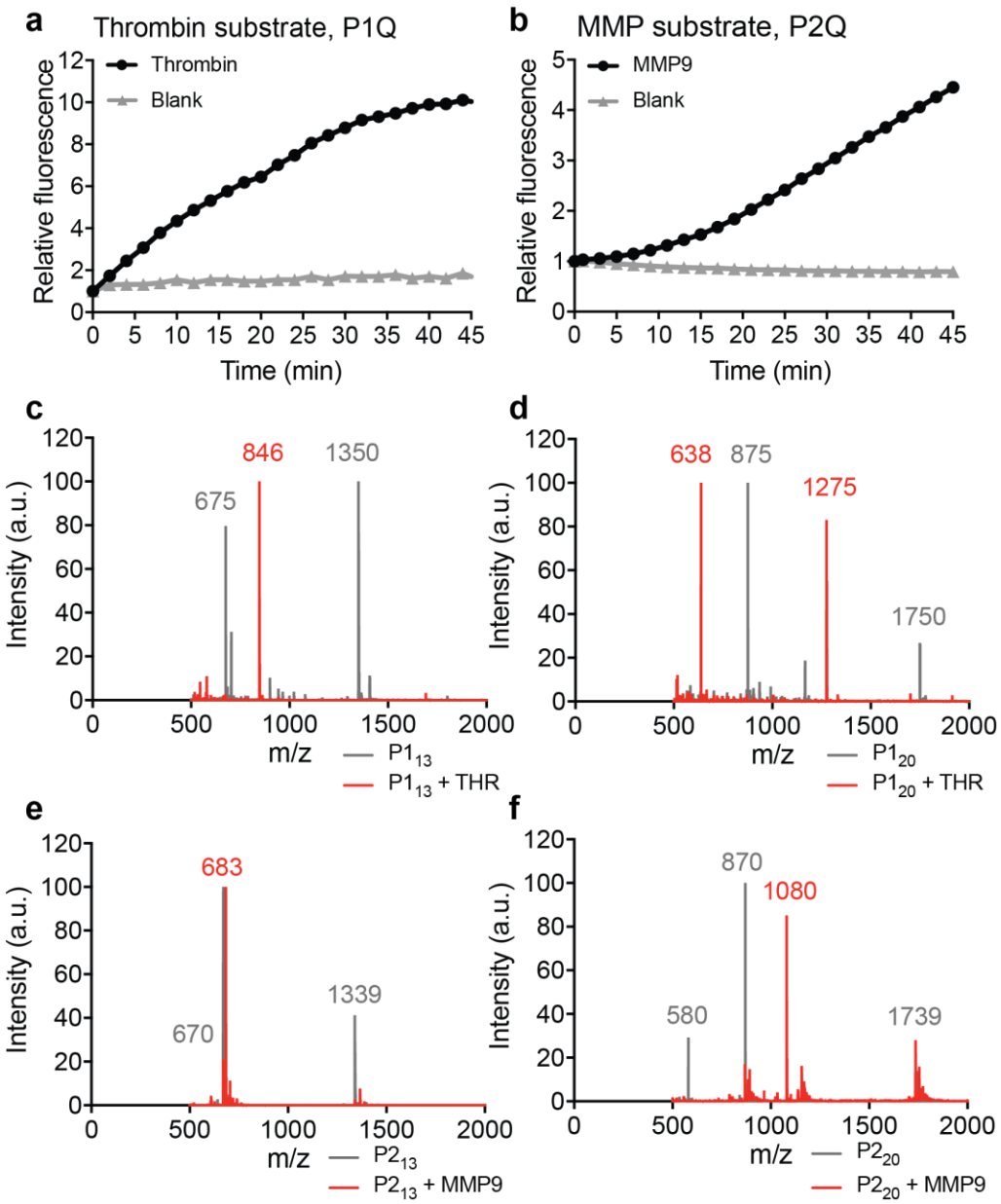

Supplementary Figure 2. Proteolytic cleavage of peptide substrates. (a) and (b) Fluorescently quenched thrombin- or MMP-responsive (a and b, respectively) peptides were incubated with target enzyme (human thrombin or human MMP9, respectively). Proteolytic cleavage released the quencher, and fluorescence was measured to monitor cleavage kinetics (mean, n = 2 independent measurements). (c) and (d) Liquid chromatography-mass spectrometry (LC-MS) chromatograms of thrombin-responsive $P1_{13}$ and $P1_{20}$ peptides (c and d, respectively) following 12 h incubation with recombinant thrombin, where the experiments were repeated independently 3 times with similar results. (e) and (f) LC-MS chromatograms of MMP-responsive $P2_{13}$ and $P2_{20}$ peptides (e and f, respectively) following 12 h incubation with recombinant MMP9, where the experiments were repeated independently 3 times with similar results.

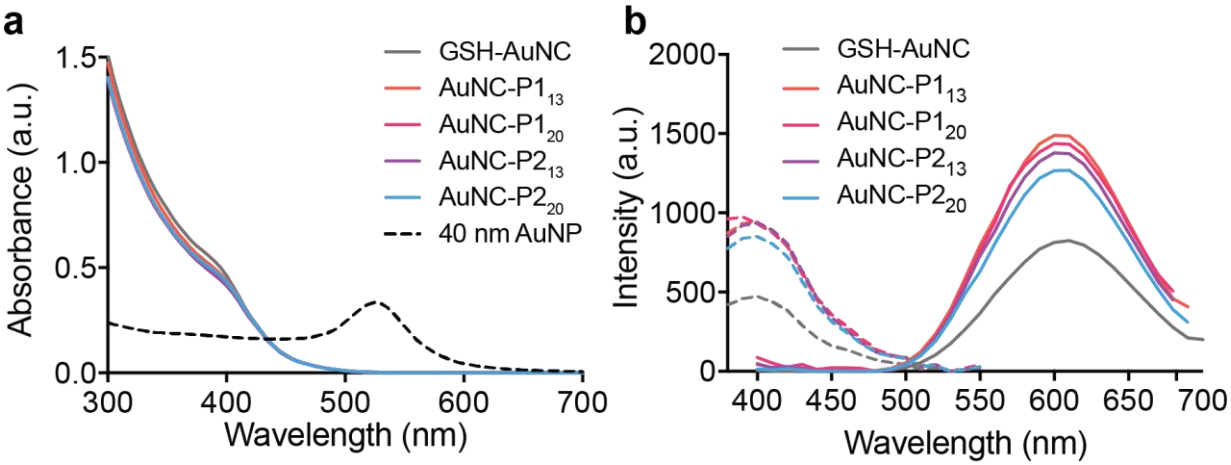

Supplementary Figure 3. Characterization of optical properties of AuNCs. (a) UV/vis absorption spectrum of peptide-templated AuNC batches compared to 40 nm gold nanoparticles (AuNPs). AuNCs did not exhibit surface plasmon resonance peak at 520 nm characteristic of larger AuNPs. (b) Fluorescence excitation (Em: 600 nm, dotted line) and emission (Ex. 400 nm, solid line) spectrum. Experiments were repeated independently 3 times with similar results.

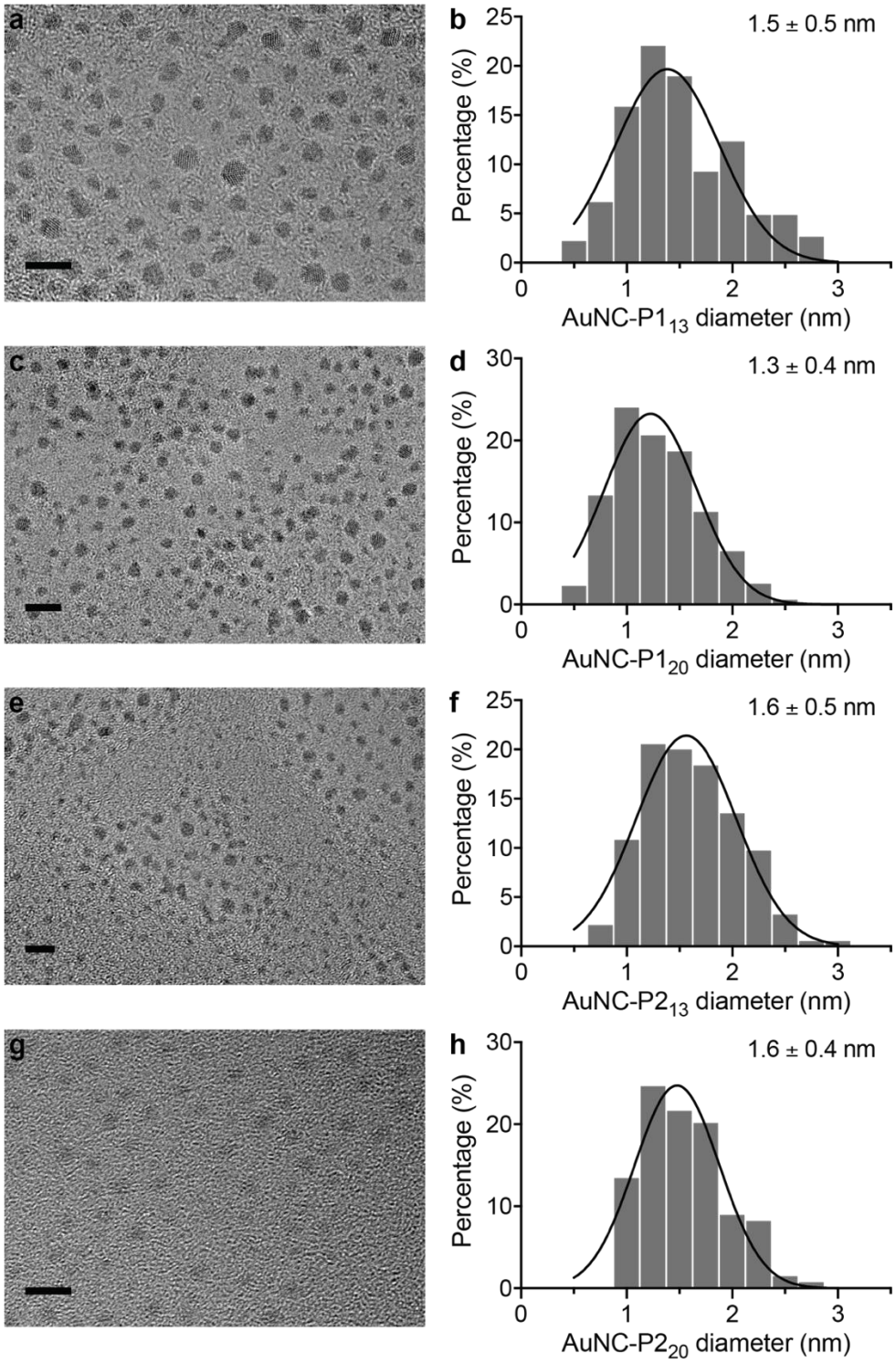

Supplementary Figure 4. Representative TEM images of AuNCs synthesized with different peptide sequences and corresponding particle size analysis. (a, b) AuNC-P1$_{13}$, (c, d) AuNC-P1$_{20}$, (e, f) AuNC-P2$_{13}$, (g, h) AuNC-P2$_{20}$. Scale bars, 5 nm; legends in b (n = 227), d (n = 354), f (n = 185), and h (n = 134) show mean diameter ± s.d.

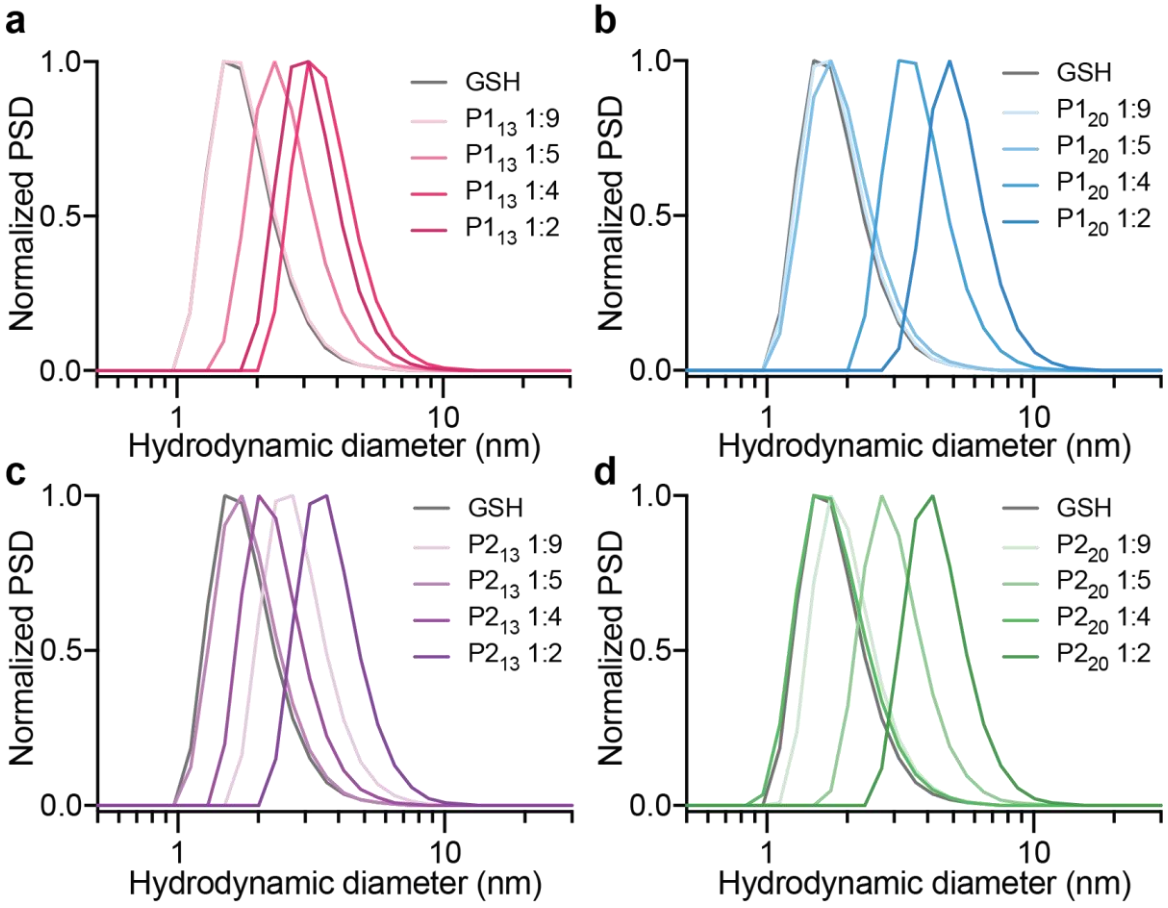

Supplementary Figure 5. Number particle size distribution (PSD) measured by dynamic light scattering (DLS) of AuNCs synthesized with different peptide sequences (a) $P1_{13}$, (b) $P1_{20}$, (c) $P2_{13}$, (d) $P2_{20}$. Increasing intensity of coloured line corresponds to increasing concentration of protease-cleavable peptide sequence in synthesis. Ratios in legends correspond to the PX:glutathione ratio (1:9, 1:5, 1:4, 1:2) used in synthesis. All particles were synthesized with a fixed total peptide concentration and DLS experiments were repeated independently 3 times with similar results.

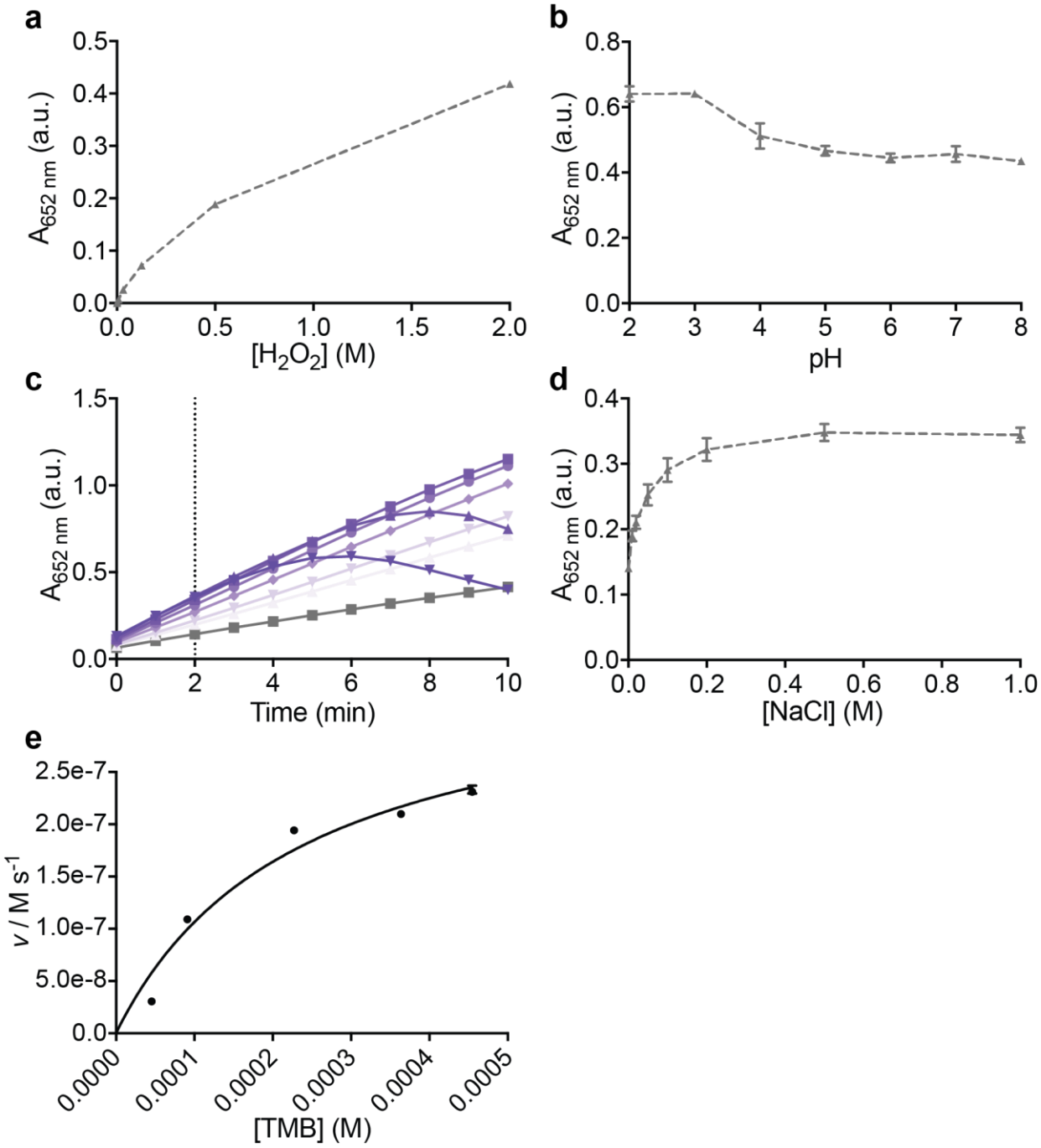

Supplementary Figure 6. Characterization and optimization of catalytic activity assay conditions. (a) Catalytic activity of GSH-AuNCs as a function of hydrogen peroxide concentration (mean ± s.d., *n* = 3 independent experiments). Activity was measured by the absorbance at 652 nm corresponding to the oxidation of TMB by H_2O_2. Colorimetric signal increased with increasing concentration of hydrogen peroxide in assay buffer. (b) Catalytic activity of GSH-AuNCs as a function of pH (mean ± s.d., *n* = 3 independent experiments). (c) Kinetic measurement of catalytic activity with varying sodium chloride concentration (gray: no salt; increasing colour intensity: 0.01, 0.02, 0.05, 0.1, 0.2, 0.5, 1 M NaCl), where precipitation of substrate occurred at high [NaCl]. Experiment was repeated independently 3 times with similar results. (d) Catalytic activity with varying [NaCl] after 2 min development (dotted line in Supplementary Fig. 6c, mean ± s.d., *n* = 3 independent experiments). PBS spiked with

ca. 2.5 M H_2O_2 was selected as the assay reaction buffer due to its neutral pH and optimal salt concentration. (e) Steady-state kinetic assays of GSH-AuNCs as catalysts for the oxidation of TMB by H_2O_2 (mean ± s.d., n = 3 independent experiments). The initial reaction velocity (v) was measured in 25 mM sodium acetate buffer pH 4.0 with 1.8 x 10^{-6} M AuNCs at room temperature over 150 seconds. Plot of v against TMB concentration, in which H_2O_2 was fixed at 2.3 M.

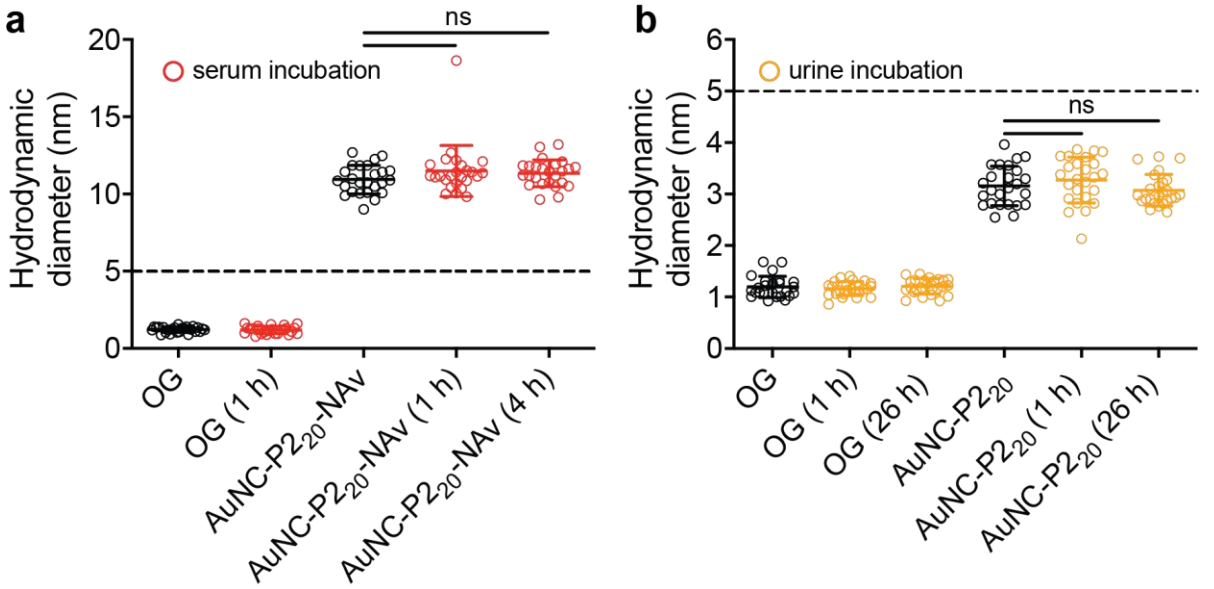

Supplementary Figure 7. Hydrodynamic diameters calculated from FCS autocorrelation curves showing sizes of Oregon Green (OG) fluorescent dye, AuNC-NAv complexes, and AuNCs after incubation in PBS (black) or physiological environments (red or yellow). (a) AuNC-P2$_{20}$-NAv complex incubated in PBS (black) or 10 % v/v fetal bovine serum (FBS, red) for 1 h and 4 h (one-way ANOVA with Dunnett's multiple comparison, ^{ns}P = 0.187 for 1 h, ^{ns}P = 0.382 for 4 h). (b) AuNC-P2$_{20}$ incubated in PBS (black) or undiluted synthetic urine (yellow) for 1 h and 26 h (one-way ANOVA with Dunnett's multiple comparison, ^{ns}P = 0.470 for 1 h, ^{ns}P = 0.657 for 26 h). Dashed line represents renal filtration size cut-off of *ca.* 5 nm. Individual sample measurements are represented as open circles with overlaid mean and standard deviation (n = 25 independent measurements).

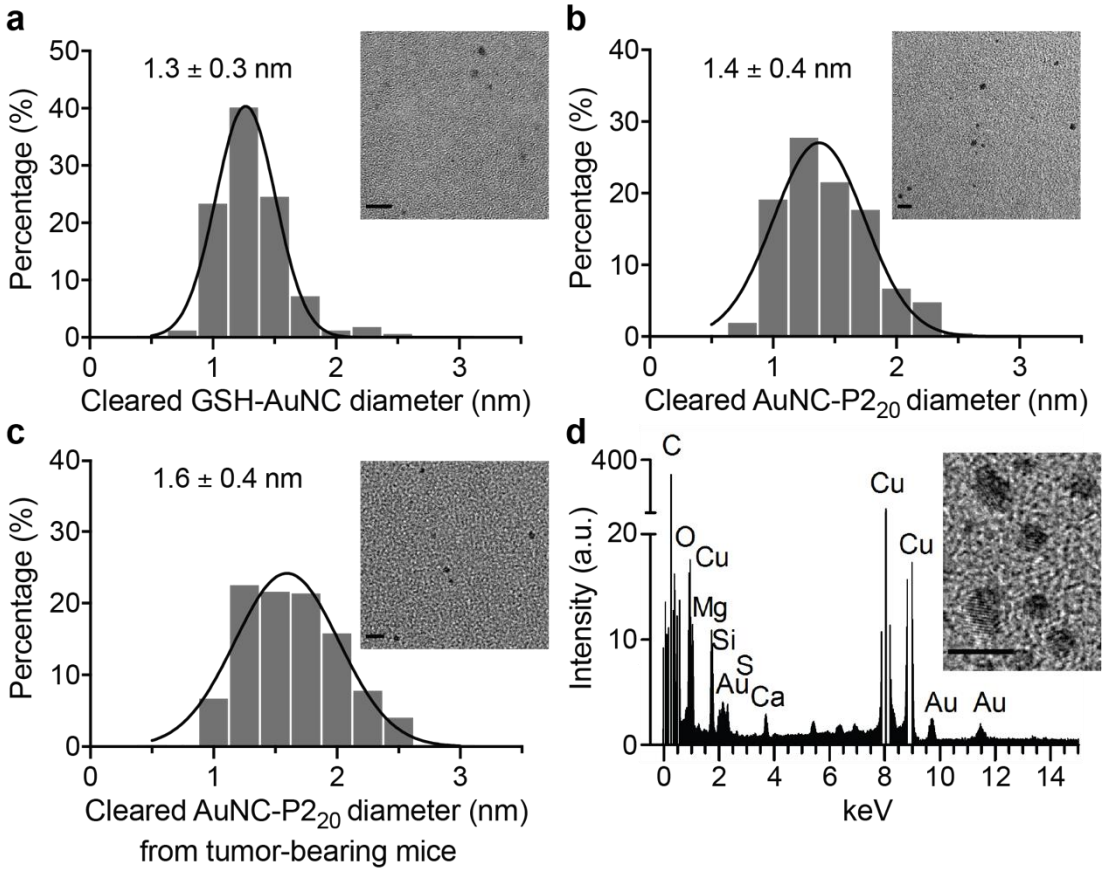

Supplementary Figure 8. Characterization of AuNCs in urine after kidney filtration. Histogram showing results of size analysis from TEM images of (a) GSH-AuNCs (legend shows mean diameter ± s.d., *n* = 167 particles) and (b) AuNC-P2$_{20}$ (*n* = 209 particles) in mouse urine that was collected 1 h p.i. with AuNC samples. (c) AuNCs in mouse urine 1 h p.i. of MMP9-responsive AuNC-P2$_{20}$-NAv complexes in tumour-bearing mice, indicating successful cleavage and renal elimination of liberated AuNCs in tumour model (*n* = 449 particles). Solid line represents Gaussian fit of size distribution. Inset shows representative TEM images used for size analysis for each particle batch (scale = 5 nm). AuNC samples in urine were desalted and purified through centrifugal ultrafiltration prior to imaging. (d) Energy Dispersive X-ray (EDS) point spectra analysis of the elemental composition of randomly selected areas across TEM grids containing cleared GSH-AuNCs in urine, where the experiment was repeated independently 3 times with similar results. EDS spectrum confirms the presence of gold and other elements that may be excreted by the kidneys, including calcium and magnesium, in addition to copper, carbon, and silicon signal from the TEM grid. Inset shows representative TEM image of grid area used for EDS analysis showing lattice fringes on AuNCs (scale = 5 nm).

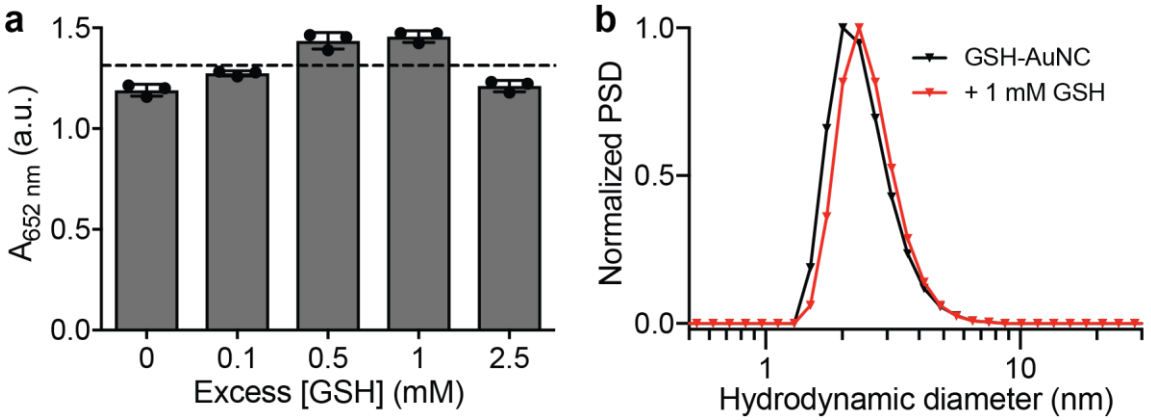

Supplementary Figure 9. Stability of AuNCs in presence of physiological glutathione concentrations. (a) Catalytic activity of GSH-AuNCs incubated with excess glutathione up to 2.5 mM for 1 h at 37 ºC. The dashed line indicates the average catalytic activity measured as absorbance at 652 nm corresponding to the oxidation of TMB across all samples analysed (mean ± s.d., *n* = 3 independent experiments). (b) Number particle size distribution (PSD) measured by DLS of GSH-AuNCs in PBS (black) and GSH-AuNCs incubated in the presence of 1 mM glutathione for 1 h at 37 °C (red), where the DLS experiment was repeated independently 3 times with similar results.

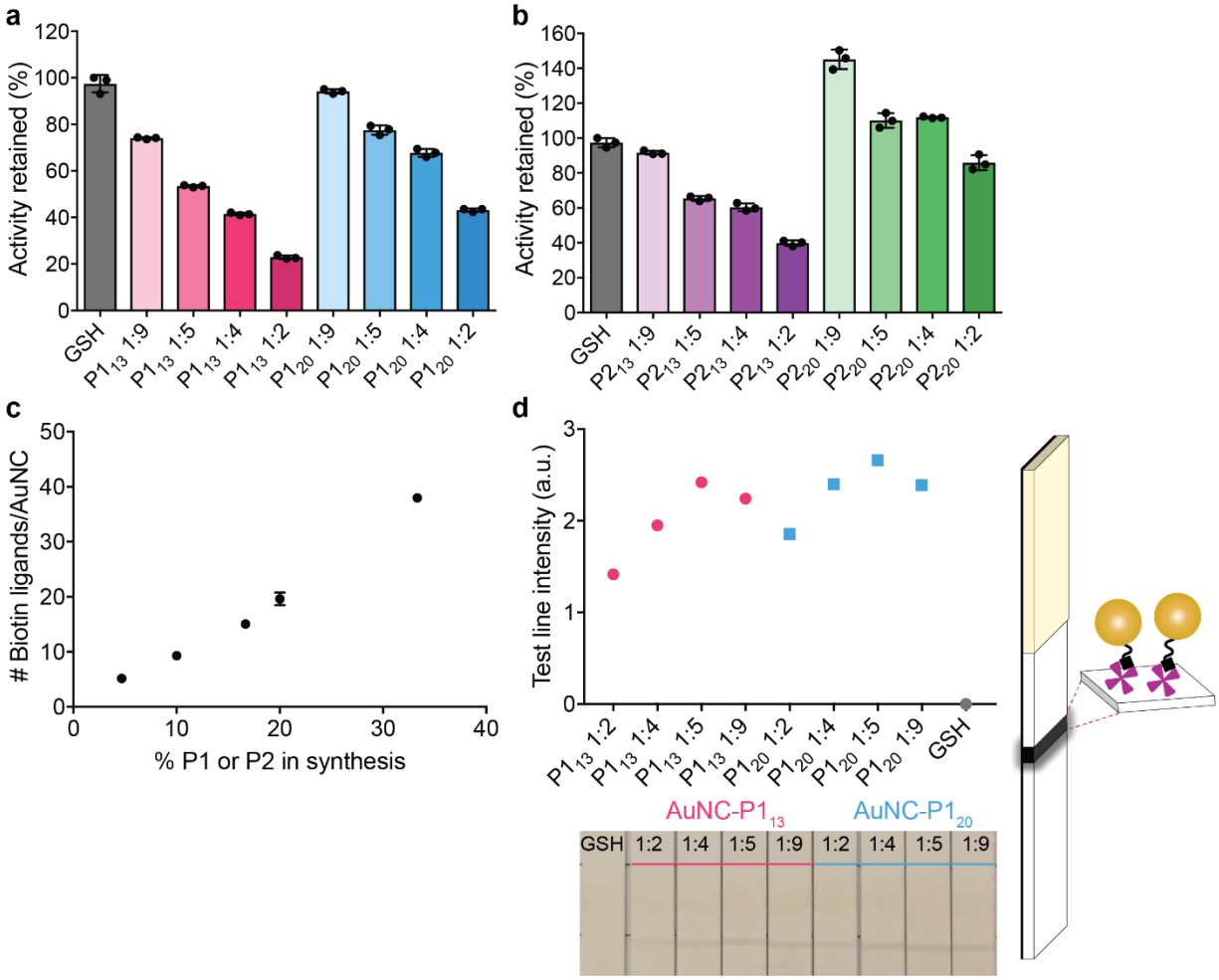

Supplementary Figure 10. Characterization of AuNCs functionalised with protease-responsive peptides. (a, b) Catalytic activity of AuNCs synthesized with varying protease-cleavable peptide sequences ($P1_{13}$, $P1_{20}$, $P2_{13}$, $P2_{20}$) and varying ratios of protease-cleavable peptide sequence to glutathione (PX:glutathione in ratios 1:9, 1:5, 1:4, 1:2), where activity is normalized to activity of AuNCs synthesized in the absence of $P1_{13 \text{ or } 20}$, $P2_{13 \text{ or } 20}$ (glutathione only, GSH-AuNCs). Activity decreased with increasing amount of P1 or P2 incorporated onto the AuNC surface. This change could be ascribed to the bulkier peptides replacing GSH in the synthesis, which may block access to the AuNC surface, decreasing surface area available for interaction with substrate molecules and subsequent catalytic reactions. The biotinylated protease substrate is required to form the AuNC-NAv complex; however, increasing the number of P1 or P2 peptides per AuNC resulted in a decrease in activity, thus requiring a careful balance of synthesis parameters. The differences in catalytic activity with varying peptide sequence may be attributed to variations in peptide hydrophobicity, charge, and molecular weight affecting accessibility and affinity of substrate molecules for the catalytic surface. (c) Quantification of biotin ligands per AuNC when ratio of peptide sequence ($P1_{13 \text{ or } 20}$, $P2_{13 \text{ or } 20}$) to glutathione was varied in the synthesis. Amount of biotin in supernatant of AuNC synthesis after purification was measured using 4'-hydroxyazobenzene-2-carboxylic acid (HABA)-avidin reagents, and biotin concentration on the particles was extrapolated using the starting concentration of biotin in synthesis and estimated concentration of AuNCs. (d) The functional performance of the AuNC batches containing different ratios of the protease-cleavable substrates on the surface was tested using a paper-based assay (schematic on right).

The assay used a streptavidin test line to measure the ability of the AuNC to effectively bind to avidin and a subsequent catalytic development step to probe the activity of the particles. We found that there was an optimal ratio of protease substrate incorporated in the synthesis which led to efficient capping of the gold core with biotinylated protease cleavable ligands while retaining activity to preserve diagnostic sensitivity (1:5 ratio for thrombin substrates (P1) and a 1:4 ratio for MMP substrates (P2), which is taken forward in synthesis of particles in the following figures). The optimal substrate incorporation for efficient synthesis corresponded to *ca*. 15 – 20 biotinylated protease substrates per AuNC, where *ca*. 20 % ligands are protease-cleavable peptides and the remaining capping ligands are glutathione. Test line intensity quantified in ImageJ corresponding to AuNC-P1$_{13 \text{ or } 20}$ binding to polystreptavidin test line, where the experiment was repeated independently 3 times with similar results. AuNCs bound at the test line catalyze the oxidation of CN/DAB (4-chloro-1-naphthol/3,3′-diaminobenzidine tetrahydrochloride) substrate in the presence of hydrogen peroxide producing an insoluble black product. All error bars indicate mean ± s.d., n = 3 independent experiments.

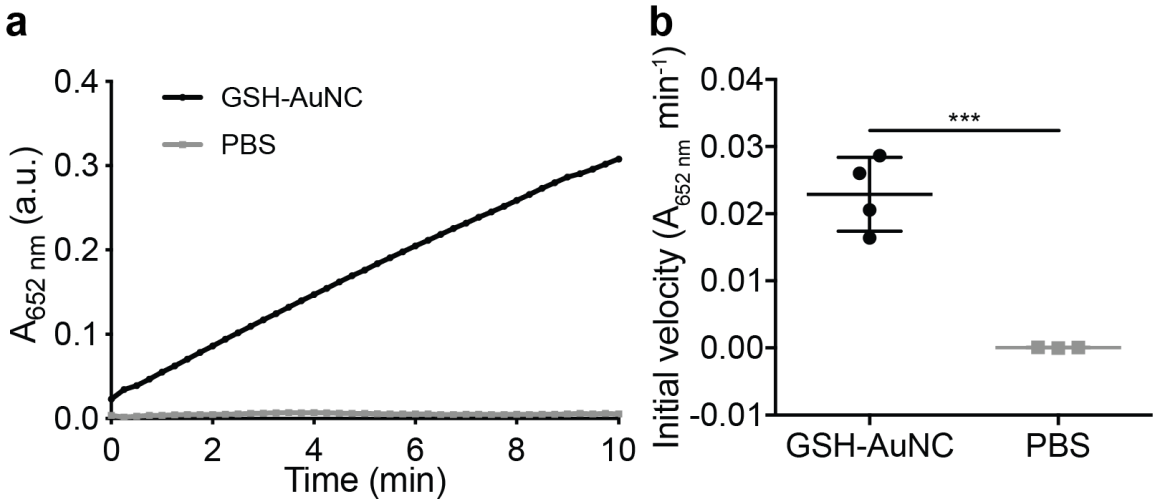

Supplementary Figure 11. Assessment of endogenous peroxidase activity in mouse urine. (a) Representative kinetic measurement of catalytic activity in urine samples of mice injected with GSH-AuNCs or PBS. (b) Quantification of initial velocity of catalytic activity from (a), as measured by the rate of change of $A_{652\ nm}$ over the first 10 minutes of the reaction (mean ± s.d., n = 3 mice for PBS injection and n = 4 mice for GSH-AuNC injection, two-tailed Student's t-test, ***P = 0.0009).

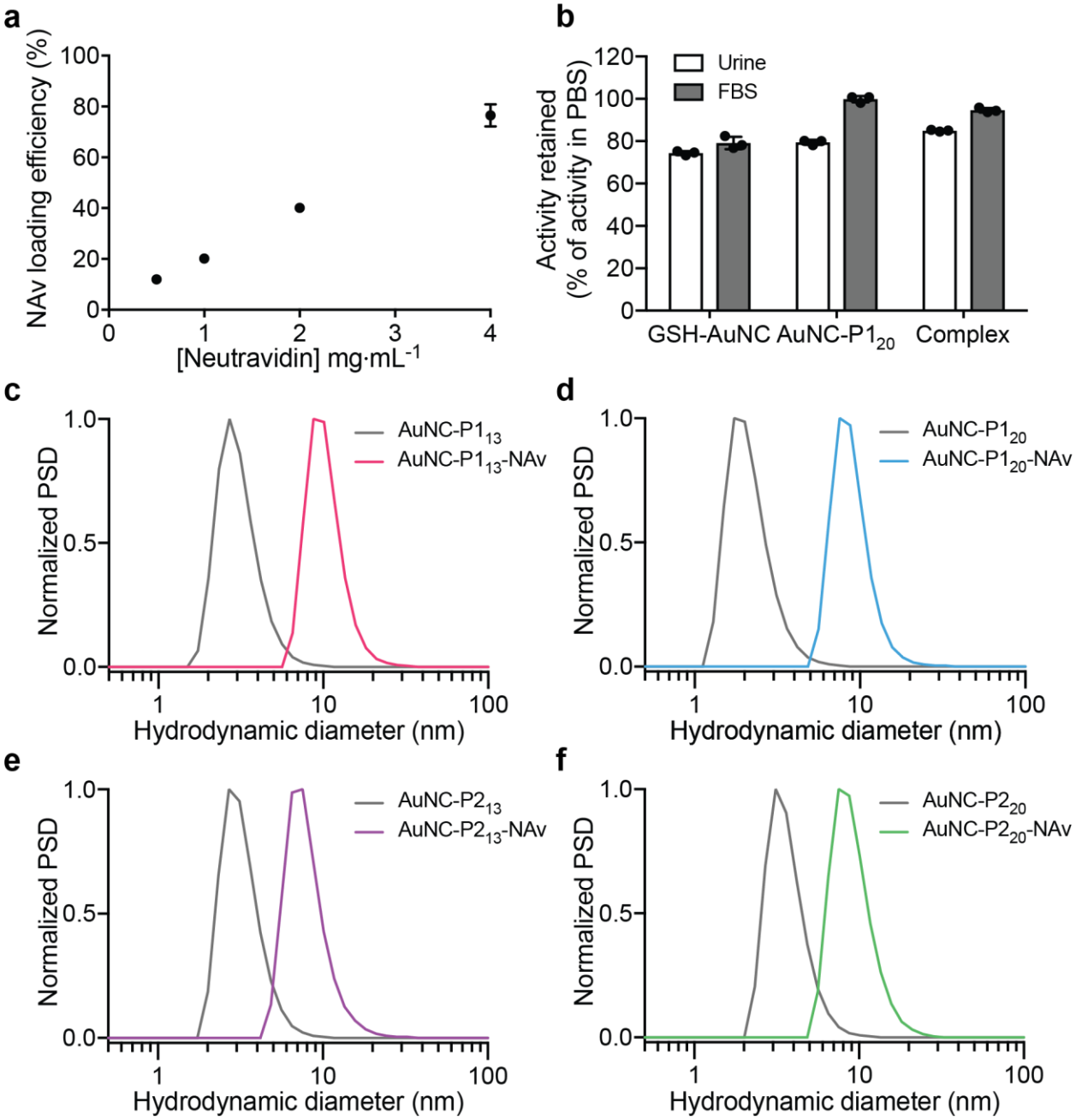

Supplementary Figure 12. Synthesis efficiency, serum stability, and size characterization of AuNC-NAv complexes. (a) Quantification of efficiency of binding of biotinylated AuNCs to neutravidin protein for varying neutravidin concentrations, where 4 mg·mL^{-1} represents a 1.2 molar excess of AuNCs to neutravidin carrier protein, and 0.5 mg·mL^{-1} represents a 9.6 molar excess of AuNCs to neutravidin (mean ± s.d., *n* = 3 independent experiments). Loading efficiency was measured by calculating the difference in catalytic activity of AuNC-NAv complex before and after ultrafiltration purification to remove unbound AuNCs. Incubation with higher concentrations of neutravidin increased the efficiency of complex formation by up to 70 %. While theoretically four biotins should be able to simultaneously bind one neutravidin carrier, it was not possible to load more than two AuNCs on a neutravidin core, even with a large excess of AuNCs (10 molar excess of AuNCs to protein). This could be in part due to steric hindrance. Each AuNC has *ca*. 20 biotin ligands, so it is also possible that one AuNC could exhibit multivalent binding to the neutravidin core.

(b) Catalytic activity of AuNCs and AuNC-NAv complex after incubation in urine (undiluted) or fetal bovine serum (undiluted FBS) environments for 1 h. Activity was normalized to activity of sample in PBS (mean ± s.d., *n* = 3 independent experiments). (c-f) Number particle size distribution of hydrodynamic diameter measured by DLS for AuNC-$P1_{13}$, -$P1_{20}$, -$P2_{13}$, -$P2_{20}$ and corresponding AuNC-NAv complexes prepared with each particle batch after purification. DLS experiments were repeated independently 3 times with similar results.

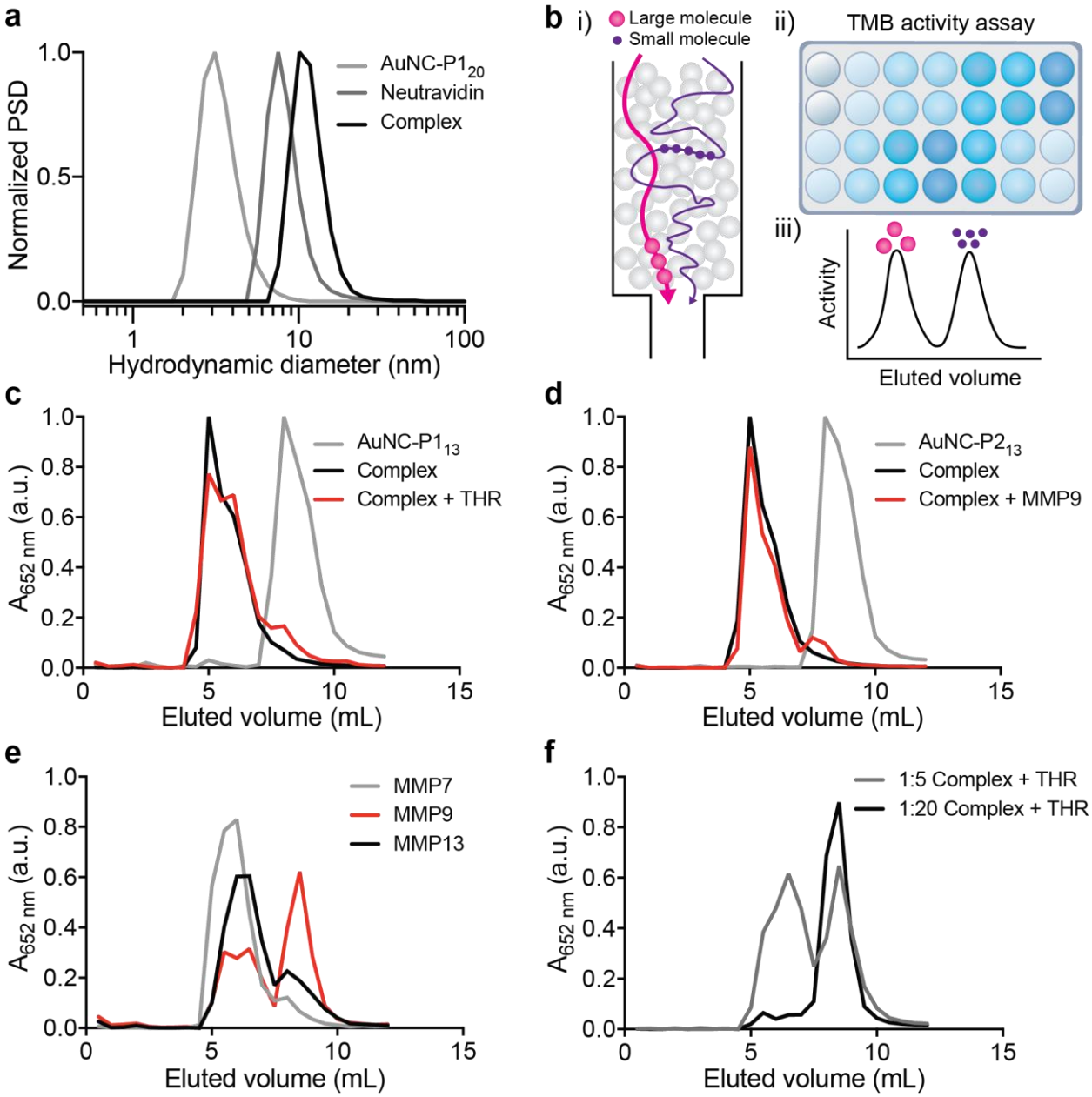

Supplementary Figure 13. Gel filtration chromatography (GFC) analysis for monitoring AuNC-NAv complex dissociation. (a) Number distribution of the hydrodynamic diameter of AuNC-P1$_{20}$, neutravidin protein, and AuNC-NAv complex (Complex) measured by DLS. (b) Schematic of *in vitro* assay to monitor size of AuNC-NAv complex in response to recombinant protease activity. (i) Gel filtration chromatography is used to separate molecules based on size (free AuNCs are smaller than AuNC-NAv complex). (ii) Catalytic activity assay is performed on collected column fractions. (iii) Activity of column fractions can be plotted against eluted volume and area under curve can be used to determine ratio of free AuNCs to complex. (c) AuNC-P1$_{13}$, AuNC-P1$_{13}$-NAv complex (Complex), and 10 µM AuNC-P1$_{13}$-NAv complex incubated with 50 nM thrombin for 12 h at 37 °C (Complex + THR). (d) AuNC-P2$_{13}$, AuNC-P2$_{13}$-NAv complex (Complex), and 10 µM AuNC-P2$_{13}$-NAv complex incubated with 50 nM MMP9 for 12 h at 37 °C (Complex + MMP9). (e) AuNC-P2$_{20}$-NAv complex incubated with 50 nM MMP7, MMP9, or MMP13 for 12 h at 37 °C. The MMP-responsive nanosensor was cleaved more robustly by MMP9 (gelatinase) than

by MMP7 (matrilysin) or MMP13 (collagenase). (f) Activity of GFC column fractions for AuNC-NAv complexes prepared with different $P1_{20}$ loadings ($P1_{20}$:GSH 1:5 or 1:20), where 1:5 case has *ca*. 20 biotin ligands per AuNC and 1:20 case has *ca*. 5 biotin ligands per AuNC, for 1 h incubation with 50 nM thrombin at 37 °C. We hypothesized that by reducing the number of biotin ligands on the AuNC surface, we would have a higher probability of an enzyme cleavage event specifically liberating an AuNC from the complex, rather than cleaving off peptides that are not actively tethering the AuNC to the core. Indeed, we did see this effect, where for AuNCs with only 5 biotin ligands per cluster we observed *ca*. 40 % more cleavage than for AuNCs presenting 20 biotin ligands per cluster for 1 h incubation with 50 nM thrombin. However, forming the AuNC-NAv complex is over twice as efficient when the AuNCs present 20 biotin ligands per AuNC, so we maintained this loading for the current study. All DLS and GFC experiments were repeated independently 3 times with similar results.

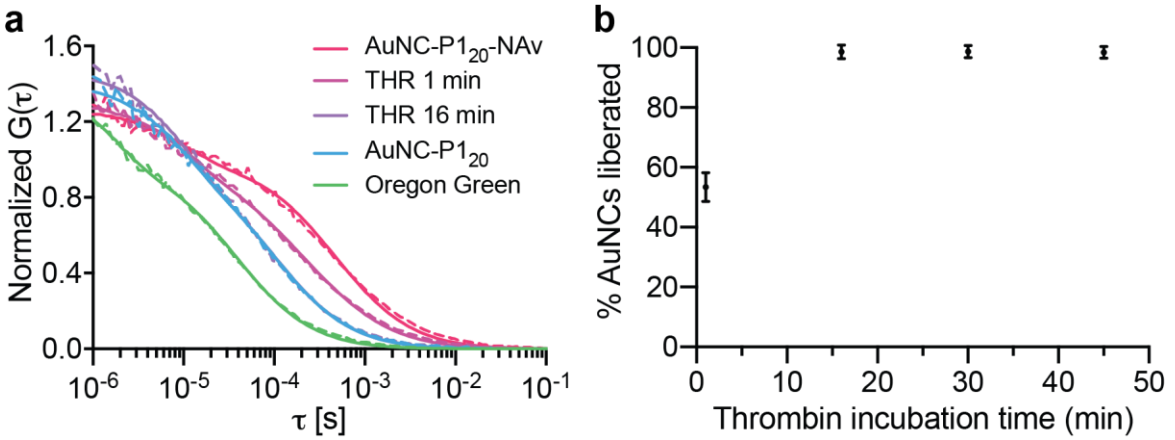

Supplementary Figure 14. (a) Average autocorrelation curves from FCS measurements (n = 25 independent measurements) showing AuNC-P1$_{20}$-NAv complex in the presence of thrombin over time compared to free labelled AuNCs and Oregon Green dye (dashed lines: experimental; solid lines: fits). A clear shift to faster diffusion times was observed for longer enzyme incubation times where the complex incubated with thrombin for 16 min (purple) overlaps with the AuNC-P1$_{20}$ curve (blue), indicating complete cleavage of AuNCs from the complex in this timeframe. (b) Plot of fraction of AuNCs liberated (see FCS in Methods) from AuNC-P1$_{20}$-NAv complex incubated with thrombin (50 nM) up to 45 min. (mean ± s.d., n = 25 independent measurements).

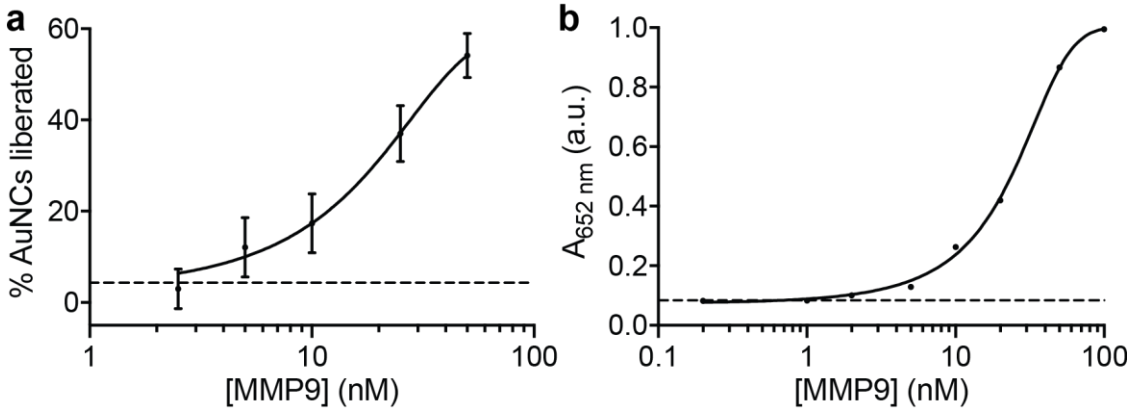

Supplementary Figure 15. Probing MMP9 *in vitro* limit of detection. (a) Plot of fraction of AuNCs liberated (see FCS in Methods) from AuNC-$P2_{20}$-NAv (15 µM) incubated with varying concentrations of MMP9 (2.5 – 50 nM) for 1 h to mimic *in vivo* experimental time frame (mean ± s.d., *n* = 25 independent measurements). To assemble the complexes for FCS analysis, the AuNC-$P2_{20}$ were first labelled with Oregon Green ($OG_{488\ nm}$) dye prior to forming a complex with neutravidin. Dashed line represents mean of background signal (samples spiked with PBS instead of MMP9). (b) Plot of absorbance (proportional to catalytic activity of AuNCs) of filtrate containing liberated AuNCs after incubation of AuNC-$P2_{20}$-NAv (15 µM) with varying concentrations of MMP9 (0.2 –100 nM) for 1 h to mimic *in vivo* experimental time frame (mean ± s.d., *n* = 3 independent experiments) and separated using 50 kDa cut-off centrifugal filter (pore size *ca*. 5 nm). Dashed line represents the detection cut-off calculated as 3 standard deviations above the mean of the background signal (samples spiked with PBS instead of MMP9).

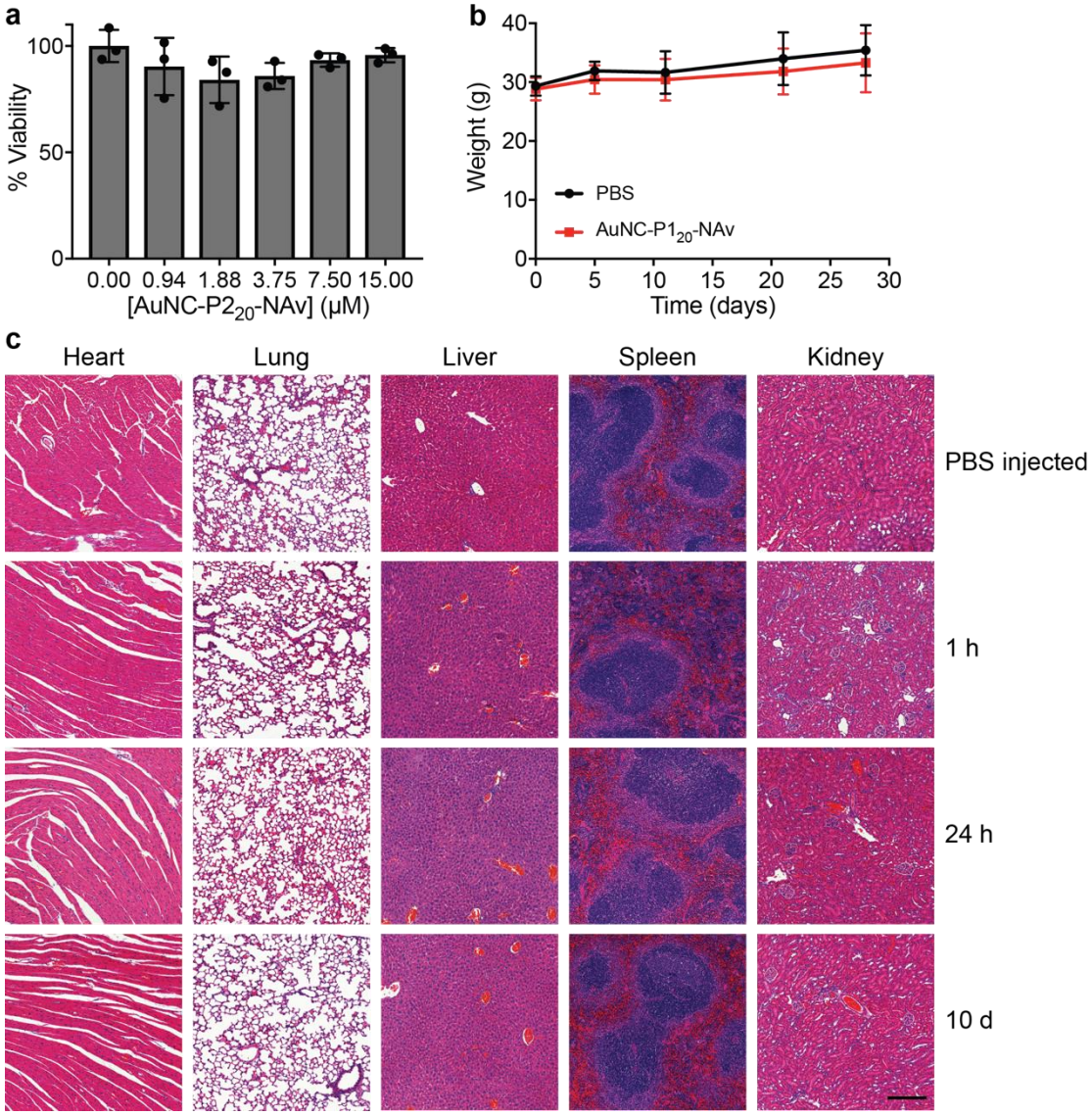

Supplementary Figure 16. Biocompatibility of AuNC-NAv complex. (a) *In vitro* cytotoxicity of AuNC-NAv complex towards HEK293T cells, determined by the MTS assay (mean ± s.d., n = 3 biologically independent samples). AuNC-P2$_{20}$-NAv at the indicated concentrations was incubated with cells for 24 h. (b) Change in body mass of immunocompetent Swiss Webster mice injected with AuNC-P1$_{20}$-NAv (dose = 3000 pmol, 200 µL of 15 µM [AuNC]) compared with PBS control (mean ± s.d., n = 4 mice per group). There was no statistically significant difference in the mass change over a period of 4 weeks between control mice (PBS injection) and mice injected with AuNC-NAv complex (multiple t-tests with Holm-Sidak correction for multiple comparisons; ^{ns}P = 0.936 for 0, 11, 21, and 28 d; ^{ns}P = 0.887 for 5 d). (c) Immunocompetent Swiss Webster mice were i.v. injected with AuNC-P2$_{20}$-NAv (dose = 3000 pmol, 200 µL of 15 µM [AuNC]) and organs (heart, lung, liver, spleen, and kidney) were collected at 1 h, 24 h, and 10 days post administration. Organs were fixed, embedded in paraffin, and stained with hematoxylin & eosin. Analysis by a veterinary pathologist confirmed that tissues from AuNC-NAv complex injected animals appeared similar to PBS injected controls, exhibiting no signs of toxicity. Study was done with n = 3 mice per group and images from representative animals are shown. Scale bar represents 200 µm.

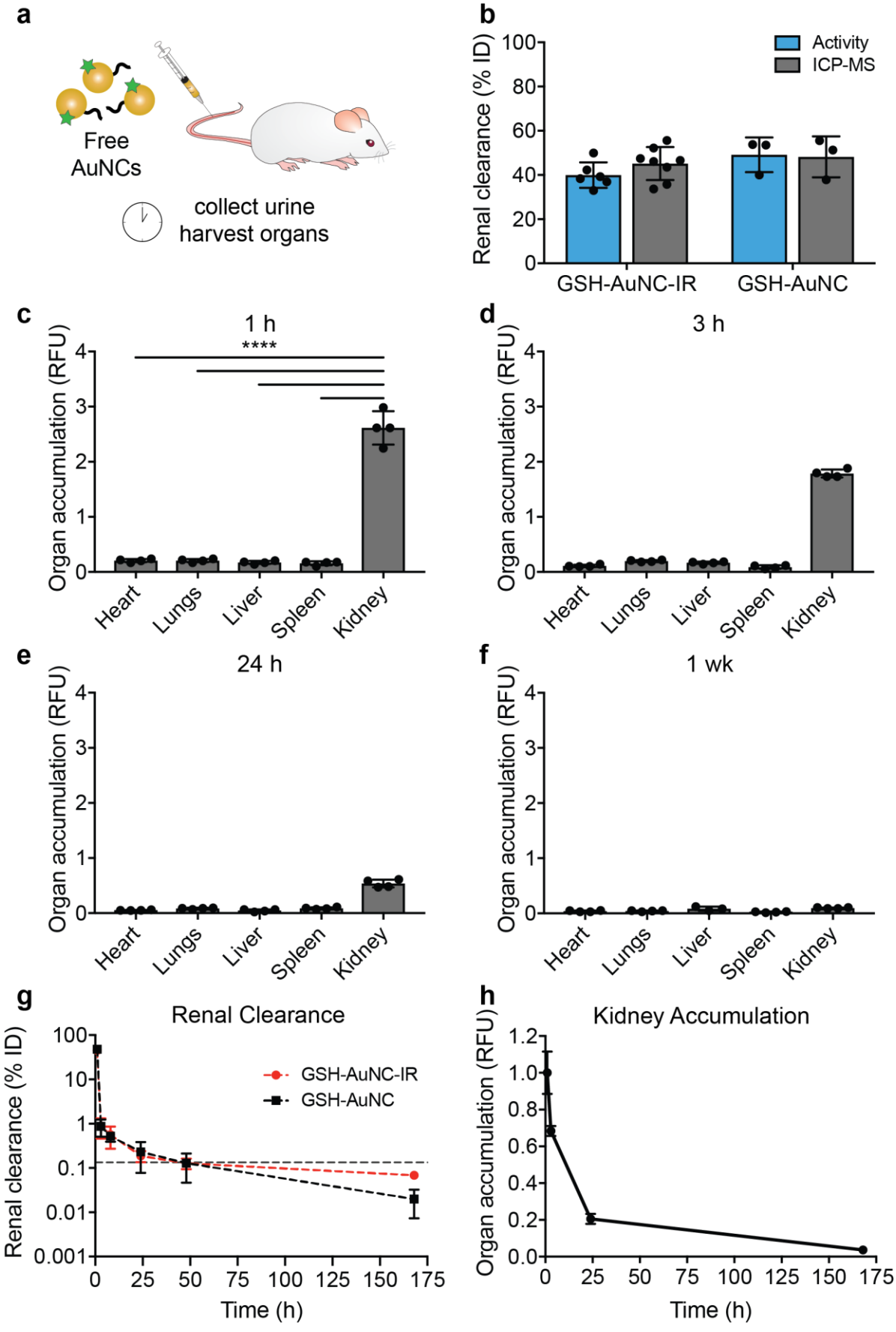
a
Free
AuNCs
collect urine
harvest organs
b
Activity
ICP-MS
Renal clearance (% ID)
GSH-AuNC-IR
GSH-AuNC
c
1 h
****
Organ accumulation (RFU)
Heart
Lungs
Liver
Spleen
Kidney
d
3 h
e
24 h
f
1 wk
g
Renal Clearance
GSH-AuNC-IR
GSH-AuNC
Time (h)
h
Kidney Accumulation

Supplementary Figure 17. Organ biodistribution and renal clearance of AuNCs in healthy mice. (a) Schematic of biodistribution and renal clearance study. Near-IR dye labelled GSH-AuNCs were i.v. injected into mice (10 µM, 200 µL), and urine samples were collected, and major organs harvested at time points up to 7 days p.i. (b) Either IR labelled GSH-AuNCs (GSH-AuNC-IR) or unlabelled GSH-AuNCs were i.v. injected into Swiss Webster mice, and urine was collected 1 h post-injection. Urine was analysed by both TMB catalytic activity assay and by ICP-MS to measure gold content, where both techniques corroborated *ca*. 47 % AuNC clearance compared to the injected dose at 1 h (mean ± s.d., n = 4 mice). (c-f) Organs were harvested (c) 1 h, (d) 3 h, (e) 24 h, and (f) 1 week after i.v. injection (10 µM, 200 µL) of near IR-dye labelled GSH-AuNCs into Swiss Webster mice, and the signal intensity in each organ was measured by an Odyssey IR scanner (mean ± s.d., n = 4 mice). Organ accumulation (y-axis) is presented as signal intensity per unit area, calculated for each organ as the difference between the experimental group (near IR-dye labelled GSH-AuNCs) versus the PBS-injected control. GSH-AuNCs accumulate significantly in kidneys 1 h post i.v. administration (one-way ANOVA with Tukey's multiple comparison test, ****P < 0.0001). Kidney accumulation is significantly reduced 1 week post administration of GSH-AuNCs, likely due to excretion of AuNCs into urine. (g) Renal clearance time course of IR labelled GSH-AuNC or unlabelled GSH-AuNC in collected urine as measured by ICP-MS (estimated ppb cleared), normalized to gold content of the injected dose (mean ± s.d., n = 4 mice). Gold content was below the limit of detection in urine after 24 h p.i., where the detection cut-off was calculated as 3 standard deviations above the mean gold signal from PBS injected control mice (cut-off = 0.13 % ID). (h) Kidney accumulation from biodistribution time course monitored up to 1 week p.i. (normalized to 1 h). AuNC signal is undetectable in kidneys at 1 week p.i. (mean ± s.d., n = 4 mice).

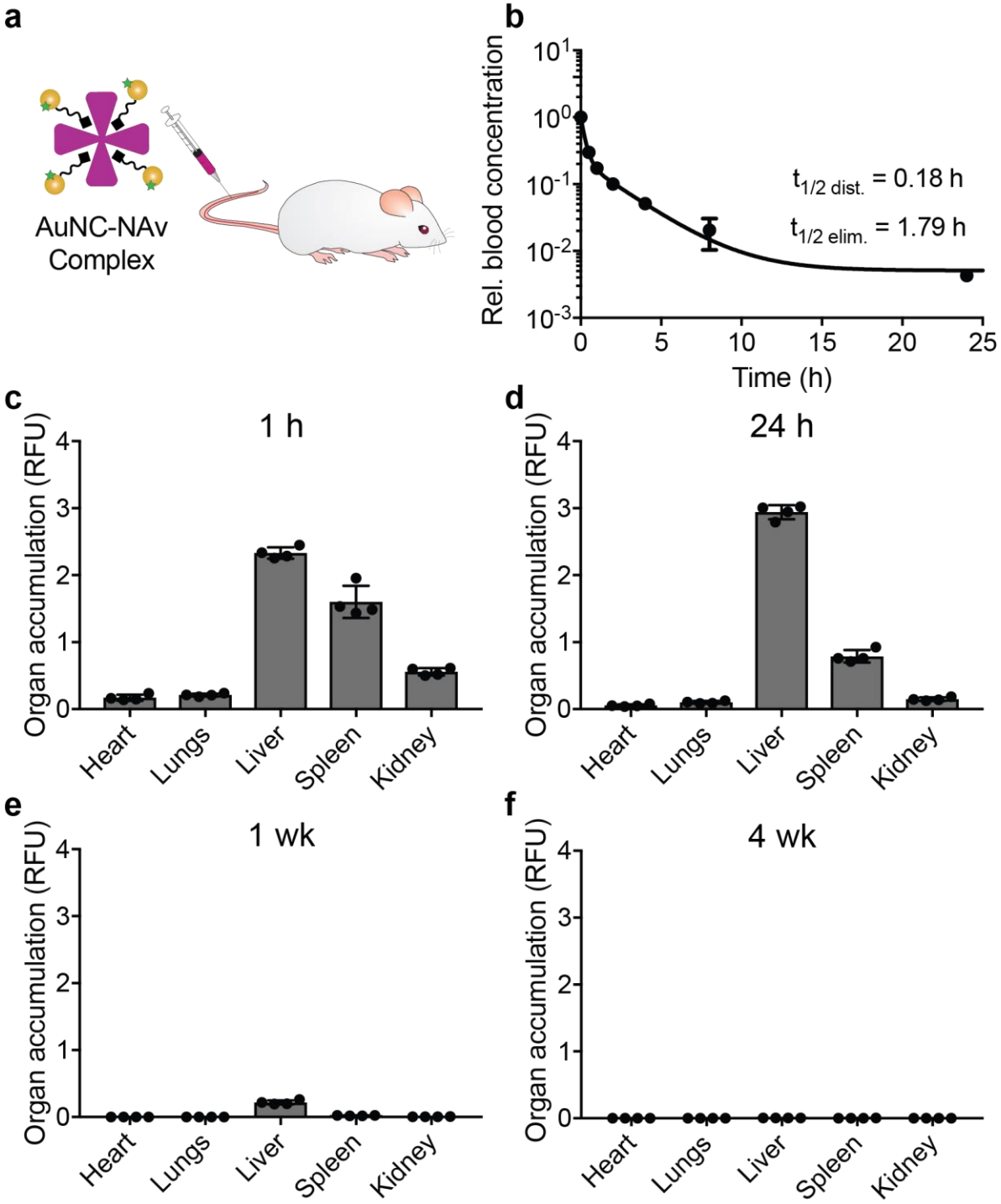

Supplementary Figure 18. Time course biodistribution of AuNC-NAv complex in healthy mice. (a) Schematic of biodistribution and pharmacokinetics study, where IR-dye labelled AuNC-$P2_{20}$-NAv complexes were i.v. injected into Swiss Webster mice (15 µM, 200 µL), and blood samples were collected, and major organs harvested at time points up to 4 weeks p.i. (b) Pharmacokinetic characterization of IR-dye labelled AuNC-$P2_{20}$-NAv complex in Swiss Webster mice. Plasma concentration of nanosensor was fit to a two-phase exponential decay (mean ± s.d., *n* = 5 mice). Organs were harvested (c) 1 h, (d) 24 h, (e) 1 week, and (f) 4 weeks after i.v. injection (15 µM, 200 µL) of near IR-dye labelled AuNC-$P2_{20}$-NAv complex into healthy Swiss Webster mice, and the signal intensity in each organ was measured by an Odyssey IR scanner (mean ± s.d., *n* = 4 mice). Organ accumulation (y-axis) is presented as

signal intensity per unit area, calculated for each organ as the difference between the experimental group (fluorescently labelled AuNC-NAv complex) versus the PBS-injected control. AuNC signal was maximum at 1 h for all organs except for the liver and was undetectable in all organs at 4 weeks p.i.

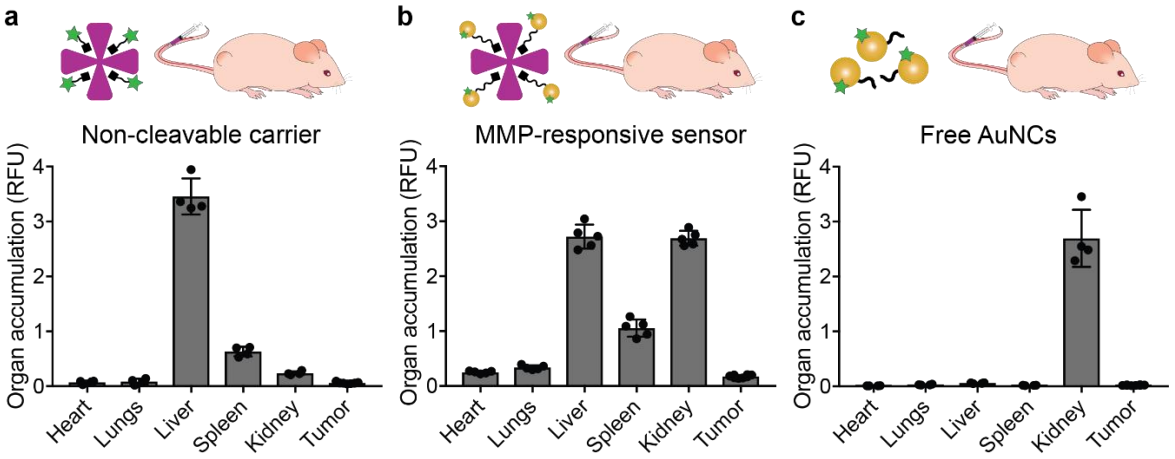

Supplementary Figure 19. Entry of AuNC nanosensor complexes into tumours at 1 h p.i. Organs and tumours were harvested 1 h after i.v. injection of near IR-dye labelled neutravidin carrier (a), MMP-cleavable AuNC-$P2_{20}$-NAv complex, where signal arises from contribution of both free AuNCs and intact AuNC-NAv complex (b), or free AuNCs (c) into LS174T tumour-bearing mice, and the signal intensity in each organ was measured by an Odyssey IR scanner (mean ± s.d., (a), (c) n = 4 mice; (b) n = 5 mice). Organ accumulation (y-axis) is presented as signal intensity per unit area, calculated for each organ as the difference between the experimental group (fluorescently labelled carrier, complex, or nanocluster) versus the PBS-injected control.

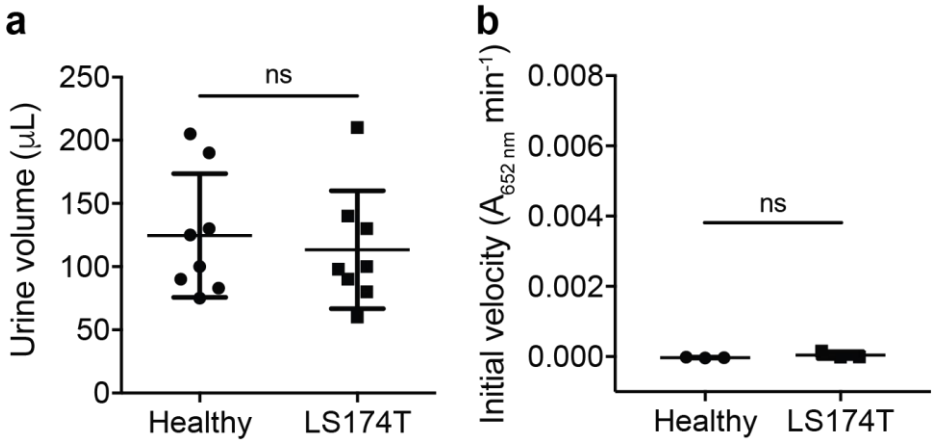

Supplementary Figure 20. Verification of colorimetric disease detection in LS174T tumour model. (a) Collected urine volumes for samples used in colorimetric disease detection experiment (Fig. 5, samples represented in black and dark blue). No statistically significant difference in urine volume was observed between the two groups (mean ± s.d., n = 8 mice per group, two-tailed Student's t-test, ^{ns}P = 0.645). (b) Catalytic activity assay on urine from healthy and tumour-bearing mice injected with PBS. No colorimetric development was observed in either group, and there was no statistically significant difference between the two groups (mean ± s.d., n = 3 mice per group, two-tailed Student's t-test, ^{ns}P = 0.284).

Supplementary Table 1. Sequences of all peptides employed in study. Lowercase indicates d-stereoisomer. Q indicates a quenched substrate with the FAM-CPQ2 FRET pair, where 5FAM is the fluorophore and CPQ2 is the quencher.

Substrate ($P_{\#aa}$)	**Protease specificity**	**Sequence (↓ represents scissile bond, enzyme recognition motif bolded.)**
P1Q	Thrombin	(5FAM)-GG **fPR**↓SGGGK(CPQ2)-(PEG2)-C
$P1_{13}$	Thrombin	Biotin-SGG**fPR**↓SGGSGGC

$P1_{20}$	Thrombin	Biotin-GGGSGGGSGG**fPR**↓SGGGGGC
P2Q	MMP9	(5FAM)-GG **PLG**↓VRGKK(CPQ2)-(PEG2)-C
$P2_{13}$	MMP9	Biotin-GGG**PLG**↓VRGKGGC
$P2_{20}$	MMP9	Biotin-GGGGGGGGGG**PLG**↓VRGKGGC

Supplementary Table 2. Comparison of the Kinetic Parameters of Various Catalysts toward the Oxidation of TMB by H_2O_2

Catalyst	**[E] / M**	**Substrate**	**K_m / M**	**V_{max} / M s^{-1}**	**K_{cat} / s^{-1}**
AuNC *ca*. 1.5 nm	1.8×10^{-6}	TMB	2.3×10^{-4}	3.6×10^{-7}	0.20
HRP[3]	2.5×10^{-11}	TMB	4.3×10^{-4}	1.0×10^{-7}	4.0×10^{3}

[*E*] represents the catalyst concentration, K_m is the Michaelis constant, V_{max} is the maximal reaction velocity, and K_{cat} is the catalytic constant that equals V_{max}/[*E*]. Steady-state kinetic assays were carried out at room temperature in a 96-well plate with 220 µL solution with estimated path length (*l*) of 0.5 cm. 25 mM NaOAc/HOAc solution (pH 4.0) was used as the reaction buffer. For kinetic assays varying TMB concentration, AuNCs (20 µM, 20 µL) were mixed with TMB (10 µM to 1 mM, 100 µL) and H_2O_2 (5 M, 100 µL). The initial reaction velocity (*v*) was calculated by $Slope_{Initial}/(\varepsilon_{TMB\text{-}652\ nm} \times l)$, where $\varepsilon_{TMB\text{-}652\ nm}$ is the molar extinction coefficient of TMB at 652 nm, which is $3.9 \times 10^4\ M^{-1}{\cdot}cm^{-1}$. The plots of reaction velocity, *v,* against TMB concentrations were fitted using nonlinear regression of the Michaelis-Menten

equation. The kinetic parameters were calculated based on the Michaelis-Menten equation: $v = V_{max} \times [S]/(K_m + [S])$, where V_{max} represents the maximal reaction velocity, [S] is the concentration of substrate, and K_m is the Michaelis constant. V_{max} was obtained from fitting to the model using GraphPad Prism software.

Supplementary Table 3. Quantification of AuNC cleavage products from *in vitro* gel filtration chromatography assays.

AuNC-NAv complex	**% Cleavage (free AuNC fraction: 7 – 12 mL)**	**Figure reference**
AuNC-$P1_{13}$-NAv + THR (12 h)	21.8%	Fig S13c
AuNC-$P1_{20}$-NAv + THR (12 h) AuNC-$P1_{20}$-NAv + MMP9 (12 h)	90.2% 7.1%	Fig 4e
AuNC-$P2_{13}$-NAv + MMP9 (12 h)	15.2%	Fig S13d
AuNC-$P2_{20}$-NAv + MMP9 (12 h) AuNC-$P2_{20}$-NAv + THR (12 h)	75.1% 5.5%	Fig 4f
AuNC-$P2_{20}$-NAv + MMP7/9/13 (12 h)	MMP7: 12.1% MMP9: 54.9% MMP13: 29.8%	Fig S13e
AuNC-1:20-$P1_{20}$-NAv + THR (1 h) AuNC-1:5-$P1_{20}$-NAv + THR (1 h)	89.9% 49.6%	Fig S13f

Supplementary Table 4. Gold content analysis in urine as measured by ICP-MS. Urine samples collected at varying time points from mice injected with either GSH-AuNC-IR or unlabelled GSH-AuNCs (mean ± s.d., *n* = 4 mice per group). Gold signal was undetectable in urine after 24 h p.i., where limit of detection was calculated as 3 standard deviations above the mean gold signal from PBS injected control mice (cut-off = 0.13 % ID).

Time (h)	**GSH-AuNC-IR (% ID by ICP-MS)**	**GSH-AuNC (% ID by ICP-MS)**
0 – 1	45.13 ± 7.46	48.20 ± 9.23
2 – 3	0.89 ± 0.43	0.87 ± 0.36
7 – 8	0.57 ± 0.30	0.52 ± 0.13
23 – 24	0.19 ± 0.05	0.23 ± 0.15
47 – 48	0.13 ± 0.03	0.13 ± 0.08
167 – 168	0.07 ± 0.01	0.02 ± 0.01
407 – 408	--	0.02 ± 0.01

References:

1. Kapusta, P. Absolute diffusion coefficients: Compilation of reference data for FCS calibration. *PicoQuant GmbH Appl. Note* (2010).
2. Müller, P., Schwille, P. & Weidemann, T. PyCorrFit-generic data evaluation for fluorescence correlation spectroscopy. *Bioinformatics* **30**, 2532–2533 (2014).
3. Gao, L. *et al.* Intrinsic peroxidase-like activity of ferromagnetic nanoparticles. *Nat. Nanotechnol.* **2**, 577–83 (2007).